BNL-114071-2017-JA

Chemically-Tunable, All-Inorganic-Based White Light Emitting 0D-1D Heterostructures

S. Yue, Y. Zhou, S. Zou, L. Wang, H. Liu, and S. S. Wong

Submitted to Advanced Optical Materials

July 2017

Condensed Matter Physics and Materials Science Department

Brookhaven National Laboratory

U.S. Department of Energy
USDOE Office of Science (SC),
Basic Energy Sciences (BES) (SC-22)

Notice: This manuscript has been authored by employees of Brookhaven Science Associates, LLC under Contract No. DE- SC0012704 with the U.S. Department of Energy. The publisher by accepting the manuscript for publication acknowledges that the United States Government retains a non-exclusive, paid-up, irrevocable, world-wide license to publish or reproduce the published form of this manuscript, or allow others to do so, for United States Government purposes.

DISCLAIMER

This report was prepared as an account of work sponsored by an agency of the United States Government. Neither the United States Government nor any agency thereof, nor any of their employees, nor any of their contractors, subcontractors, or their employees, makes any warranty, express or implied, or assumes any legal liability or responsibility for the accuracy, completeness, or any third party's use or the results of such use of any information, apparatus, product, or process disclosed, or represents that its use would not infringe privately owned rights. Reference herein to any specific commercial product, process, or service by trade name, trademark, manufacturer, or otherwise, does not necessarily constitute or imply its endorsement, recommendation, or favoring by the United States Government or any agency thereof or its contractors or subcontractors. The views and opinions of authors expressed herein do not necessarily state or reflect those of the United States Government or any agency thereof.

Chemically-Tunable, All-Inorganic-Based White Light Emitting 0D-1D Heterostructures

Shiyu Yue,[1] Yuchen Zhou,[1] Shihui Zou,[1] Lei Wang,[1] Haiqing Liu,[1] and Stanislaus S. Wong[1,2,*]

*To whom correspondence should be addressed.

Email: stanislaus.wong@stonybrook.edu; sswong@bnl.gov

[1]Department of Chemistry, State University of New York at Stony Brook, Stony Brook, NY 11794-3400

[2]Condensed Matter Physics and Materials Sciences Division, Building 480, Brookhaven National Laboratory, Upton, NY 11973

Abstract. In this study, we initially created one-dimensional (1D) Mn^{2+}-doped ZnS (ZnS: Mn) nanowires (NWs) with a unique optical signature. Specifically, these nanostructures coupled (i) ZnS defect-related self-activated emission spanning from wavelengths of 400 nm to 500 nm with (ii) Mn^{2+} dopant-induced emission centered at ~580 nm. These doped ZnS nanostructures were initially fabricated for the first time via a template-based co-precipitation approach followed by a post-synthesis annealing process. We subsequently formed novel 1D - zero-dimensional (0D) heterostructures incorporating ZnS: Mn NWs and AET (2-amino-ethanethiol) - CdSe quantum dots (QDs) by assembling annealed ZnS: Mn NWs with AET- capped CdSe QDs as building blocks via a simple technique, involving physical sonication and stirring. Optical analyses of our heterostructures were consistent with charge (hole) and energy transfer-induced quenching of ZnS self-activated emission coupled with hole transfer-related quenching of Mn^{2+} emission by the QDs. The CdSe QD emission itself was impacted by competing charge (electron) and energy transfer processes occurring between the underlying ZnS host and the immobilized CdSe QDs. Chromaticity analysis revealed the significance of controlling *both* QD coverage density and Mn^{2+} dopant ratios in predictably influencing the observed color of our all-inorganic heterostructures. For example, white-light emitting behavior was especially prominent in composites, simultaneously characterized by (i) a 2.22% Mn^{2+} doping level and (ii) a molar compositional ratio of [ZnS: Mn^{2+}]: [AET-capped CdSe QDs]) of 1: 1.5. Moreover, using these independent chemical 'knobs', we have been able to reliably tune for a significant shift within our composites from 'cold-white' (9604 K) to 'warm-white' (4383 K) light emission.

Keywords: quantum dots, nanowires, inorganic-based heterostructures, white light emission, tunable luminescence, charge transfer and energy transfer.

TOC Figure

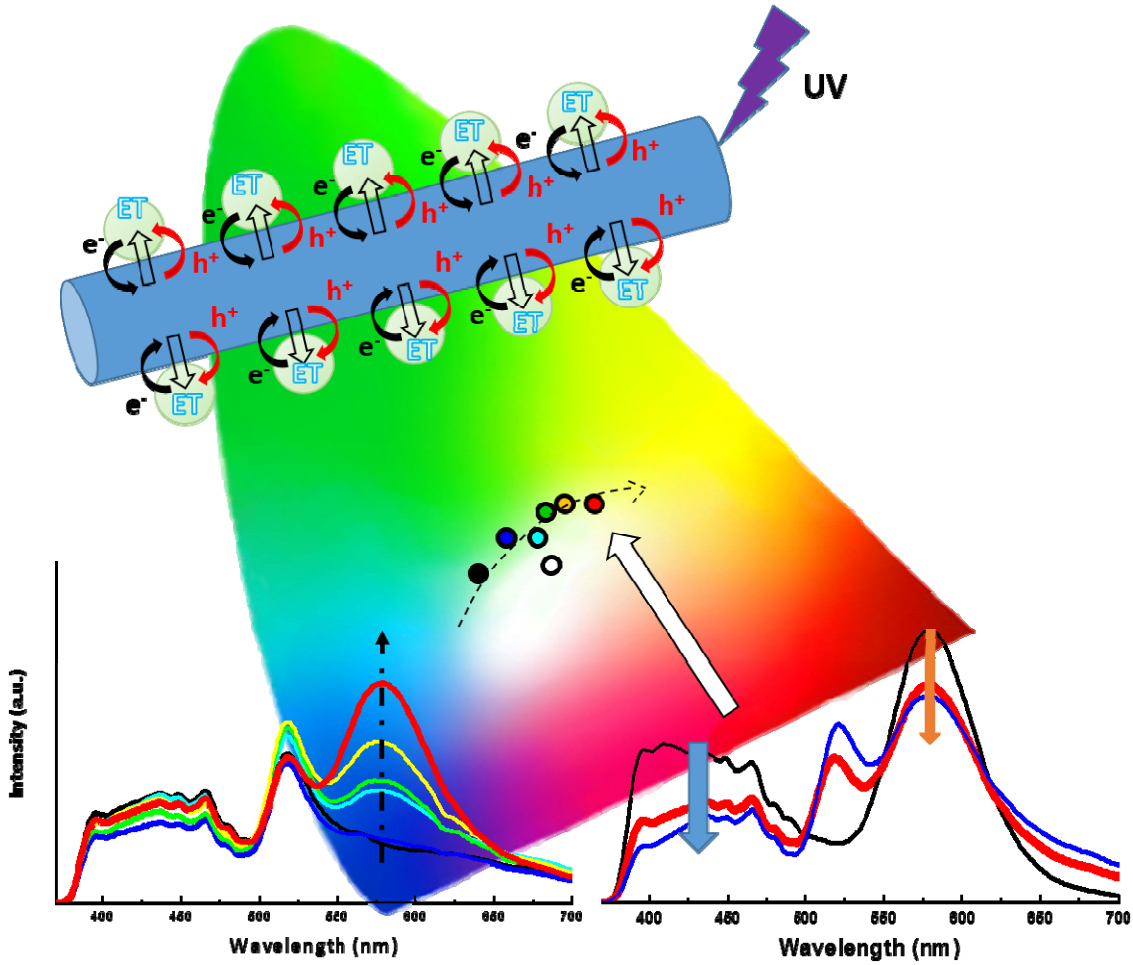
UV
ET
e-
h+
Intensity (a.u.)
Wavelength (nm)
400
450
500
550
600
650
700

1. Introduction

The optical attributes of an ideal light-emitting semiconductor would include (a) ease of tunability of its saturated color emission across the entire visible-near infrared range coupled with (b) excellent chemical and optical stability. Such a system would be highly desirable for use as components of the screen displays of personal electronic units, monitors, as well as overhead lighting units.[1] One of the most significant targets for such device applications would be the generation of a reliable white light source that would be competitive with traditional incandescent and fluorescent lighting. In effect, white light-based lighting yields key advantages, including significant power saving, longer lifetimes, higher luminous efficiency, and overall environmental compatibility.[2]

In principle, a functional white light-emitting semiconductor necessitates the generation of simultaneously excited emission bands spanning the entire visible light region, covering a wavelength range of 400 nm to 700 nm.[3] In order to satisfy these stringent optical requirements, two types of designs have been developed for white light emitters, consisting of 'single-phase' and 'multi-component' systems.[4-6] In particular, 'single-phase' white light emitters are typically composed of single-component (such as nanocrystal-based) entities that will inherently yield multi-color emissions, whereas 'multi-component' analogues characteristically give rise to a combination of color components (i.e. red, yellow, green, blue, and so forth) through incorporation of independently emitting inorganic nanocrystals and/or light emitting organic species.

Typically, 'single-phase' white emitters are generally fabricated either through doping of single or multiple types of rare-earth ions (e.g. Mn^{2+}, Eu^{2+}, Ce^{3+}or Dy^{3+})[7-11] into appropriate single-phase hosts in the absence of self-activated emission or through the mediation of 'defect-related' broad-band emissions.[12-16] For example, a 'single-phase' white-light emitting semiconductor comprised of ligand-coated ZnS: Mn quantum dots (QDs) was found to give rise to blue, green, and orange emissive behavior, derived from the collective presence of aspirin, 8-hydroxyquinoline ligands, and Mn^{2+}

dopants, respectively.[17] By altering the relative concentrations of the light-emitting ligands in this system, the observed color could be adjusted to within or near the white color region.[17]

However, the key concept of the 'multi-component' light emitting system is a more generalized one in that the optical characteristics of the desired composite, i.e. emissive color (wavelength), intensity, and spectral broadness, can be directly managed, constructed, and tailored by the judicious control over the choice and concentration of complementary emissive 'building blocks', such as but not limited to QDs, dopants, and organic ligands. In so doing, the expectation is that deleterious phenomena such as self-absorption, color aging, and non-radiative energy transfer can be minimized and that such 'multi-component' composites can be used for applications, such as color bar codes.[4-6]

To date, most of the 'multi-component' white light-emitting composites tend to be synthesized with the use of organic chromophores. Although these materials are advantageous due to their 'light-weight' and outstanding flexibility, which enable them to be applied onto curved and textured surfaces over relatively large area coverages,[18] their performance is hindered by issues associated with short lifetimes, sophisticated and costly synthetic processes, as well as poor resistance towards water and certain organic solvents, all of which limit their practical, widespread, industrial-scale applicability.

Herein, we have constructed novel inorganic-based multi-component heterostructures incorporating both zero-dimensional (0D) QDs and one-dimensional (1D) nanocrystalline motifs as complementary and optically tunable building blocks in an effort to create a distinctive family of white light-emitting composites. Unlike previous efforts in the field, our organic linker molecules used herein solely act as structural connectors to bind together the constituent components of our heterostructures; they are not intrinsic emissive centers (such as aspirin and analogous conjugated ligands, such as 8-hydroxyquinoline). As such, the photo-physical behavior of our composite architectures, including photon absorption, exciton formation, charge carrier transfer, as well as electron and hole recombination, is primarily governed by 'tunable' interactions among the various individual inorganic

emission centers (namely, the 0D QDs, the underlying 1D ZnS host, and the Mn dopant ions, respectively) within our heterostructures.

A key motivation for constructing this unique composite architectural motif is that we subscribe to the notion that (a) the unique and desirable properties of individual nanostructures can be significantly enhanced in potentially unforeseen ways through the formation of inorganic nanoscale heterostructures composed of different, unique, and complementary constituent subunits and that (b) synthesis can be used to control structure-property correlations that impact upon phenomena such as optoelectronic behavior. As such, incorporating 1D nanomaterials within our as-synthesized heterostructures is especially useful,[19-20] because these motifs tend to retain decent mechanical strength, enviable structural flexibility, large surface-to-volume ratios, and large reactive surface areas.[21] Moreover, the most substantive feature characteristic of these anisotropic structures is an intriguing quantum confinement effect,[21] which renders them as the smallest dimensional vehicles capable of efficient transport of both electrons and optical excitations.[22]

In our particular case, we have focused on generating 1D motifs of ZnS, because ZnS is an ideal candidate optical material, maintaining known direct bandgaps of 3.72 eV for the cubic zinc blende (ZB) phase and 3.77 eV for the hexagonal würtzite (WZ) phase, in addition to a large exciton binding energy of 39 mV.[23] These key optoelectronic properties of ZnS-related materials are critical for a number of optoelectronic applications, such as but not limited to flat-panel displays, injection lasers, as well as light-emitting diodes. As for the complementary choice of 0D QDs, CdSe QDs possess interesting size-dependent absorption behavior, and are desirable, because of their very high quantum yield, good photostability, and narrow band emission.[24] Moreover, QDs have been used for fluorescent labeling in biology.[25] The resulting 1D-0D composite motif not only yields a sizeable interfacial area for 'two-way' optoelectronic interactions between the individual CdSe QD and ZnS constituent units but also provides for the possibility for unique electron transport pathways.[26-28] As such, in general, multi-dimensional nanoscale-based 0D-1D heterostructures are potentially significant

as versatile building blocks for future applications, such as but not limited to photocatalysis,[29-30] energy storage,[31] photovoltaics,[32-35] optoelectronics,[32, 36-38] molecular electronics and computational devices,[39-43] sensors,[44] biological imaging,[45-46] as well as drug delivery and therapy.[32]

We have herein focused on their potential for white light emitting devices. Therefore, in this study, we have prepared new types of QD-based heterostructures, wherein 0D CdSe QDs have been successfully anchored onto the surfaces of dual-emitting (i.e. self- and dopant-activated emitting) 1D Mn-doped ZnS (ZnS: Mn^{2+}) nanowires (NWs), in a process mediated with the use of a 2-amino-ethanethiol (AET) connective linking agent. Our architecture is unusual, as most of the prior studies had primarily focused on either attaching luminescent QDs onto materials without an intrinsic emissive behavior[47] or onto hosts with solely dopant-induced optical character.[48-50]

Hence, the novelty of our ZnS: Mn^{2+} - AET-capped CdSe QD heterostructures derives from the following distinctive attributes and advantages of our 'all-inorganic'-based system.

(i) The unique dual-emissive nature of our as-prepared ZnS: Mn^{2+} NW hosts is characterized by self-activated emissions arising not only from the ZnS host structure material but also from the presence of the Mn^{2+} dopant.

(ii) As-produced excitons are created, transferred, and recombined to create white color emission, spanning the broad band of the visible spectrum through a process that efficiently and synchronously adsorbs and emits light from three different and independently tunable luminescent centers within the resulting heterostructure.

(iii) Previous reported Mn-doped ZnS white light emitting diodes have been based on either ZnS nanocrystals or core shell quantum dot motifs.[45] Our underlying host 1D ZnS nanowires provide for a larger reactive surface area for interaction with the immobilized CdSe QDs.

(iv) Within our multi-component system, we have systematically varied both the Mn^{2+} dopant ratio as well as the QD coverage to optimize white light emitting performance.

(v) We have constructed an 'all-inorganic' emitting system as a viable alternative to conventional organic-based LED modules, which tend to be plagued by issues associated with limited lifespans and an uneven color balance.[51-52]

Specifically, in order to achieve efficient and complete coverage of the entire visible spectrum spanning from 400 nm to 700 nm within a 'multi-component' architecture, we used a host consisting of annealed 1D ZnS: Mn^{2+} NWs whose spectral profile was characterized by (a) an intrinsic direct bandgap of 3.72 eV for the cubic zinc blende phase,[53] (b) a Mn^{2+} dopant-induced *orange* emission with a peak centered at ~580 nm (associated with the $^4T_1$ to $^6A_1$ transition of Mn^{2+}),[54] as well as (c) a defect-related *blue* emission band from 400-500 nm,[55] and chemically coupled these NWs with separately-prepared 0D CdSe QDs, characterized by an average diameter of 2.3 nm with (d) a *green* emission peak situated at ~520 nm. Consequently, our resulting, doped 0D-1D heterostructures evinced a white color emission, characterized by discrete peaks located within the blue (400 to 500 nm), green (520 nm), and yellow/red (580 nm) regions, respectively, as well as an overall wavelength profile within the 400 to 700 nm range.

Those QD-based inorganic heterostructures combine and build upon the merits and advantages of both luminescent QDs and doped sulfide-based host materials, so as to yield unique and compelling optical characteristics for the composite structure that transcend the behavior of its individual components. Specifically, the intensity and wavelength (color) of emissions can be predictably and readily altered by the selection and manipulation of a multi-dimensional 'parameter space' incorporating (i) a desirable chemical composition and precise size of QDs coupled with (ii) an advantageous dopant composition and defined morphology of the inorganic host material. As such, our inorganic QD-based heterostructures can possess not only broadly tunable color emission performance but also structural durability, all of which may lead to an increase in device lifetimes under high luminance conditions, a necessary requirement for flat panel displays and imaging applications.[18]

After assembling these two individual 0D and 1D components within a discrete whole, we characterized the light emitting performance of the resulting heterostructures through (1) systematic absorption and photoluminescence (PL) emission spectroscopy measurements, coupled with (2) a chromaticity analysis. Based upon the acquired optical data, we initiated a thorough study of the charge and energy transfer mechanism, governing the observed emission, which was dictated to some degree by relative energy level band alignments among our various constituent components. Based on our data, we can likely ascribe PL quenching of the intrinsic emission of Mn^{2+} within our engineered heterostructures to hole transfer from Mn^{2+} to QDs. A similar quenching of the ZnS defect-related emission could be attributed to the synergistic effects of energy and charge transfer from the ZnS: Mn^{2+} NW host lattice to immobilized QDs on its surface. By contrast, we noted little if any enhancement of the PL output of CdSe QDs, incorporated as part of our heterostructures, and assigned this observation to competing influences of electron and energy transfer between QDs and the host NWs. Not surprisingly, the efficiencies of all of these processes and hence, the observed optical behavior depended to a large extent on the QD coverage density as well as on the Mn^{2+} dopant concentration.

Based on the results of this fundamental study, our subsequent chromaticity investigation confirmed the observation of white-light emitting properties associated with ZnS: Mn^{2+} - AET-capped CdSe QD heterostructures, specifically characterized by ZnS chemically linked together with QDs in a 1: 1.5 molar ratio, concomitant with the presence of actual Mn^{2+} doping ratios of 0.45%, 1.19%, 1.51%, 1.75%, and 2.22%. Hence, we demonstrated that by carefully tuning for QD coverage and Mn^{2+} dopant concentration, we could correspondingly dictate the observed 'chromatic color' of the resulting heterostructure. Significantly, with this approach, the integrated emissive color of our as-prepared inorganic heterostructures could be uniquely modified with chemistry so as to evince a light emitter profile spanning from "warm-white" to "cold-white".

2. Experimental Section

2.1. Synthesis

2.1.1. 1D Mn-doped ZnS NWs.

(a) Room temperature synthesis via template-mediated co-precipitation

Polycarbonate track-etch membranes of approximately 6 μm in thickness, containing pore channels measuring 200 nm in diameter, were purchased from Whatman Co., U.K. The membranes were initially treated and hydrated by immersion and sonication in deionized water for 10 minutes, so as to limit the formation of air bubbles either within their interior pore channels or on the membrane surfaces themselves. Micro-contact printed OTS-SAMs (octadecyltetrachlorosilane self-assembled monolayers) were then used as hydrophobic passivation layers[56] so as to inhibit unwanted particle formation and deposition onto the external surfaces of the polycarbonate (PC) membranes. Specifically, a homemade PDMS (polydimethylsiloxane) stamp was initially inked with a 10 mM hexane solution of OTS and dried in air. The stamp was then placed into contact with the external surface of the PC membranes for 30 s, and then carefully peeled off.

Subsequently, the template membrane was mounted between the two half arms of a U-tube shaped apparatus (Figure S1). Purchased precursors of Na_2S (Alfa Aesar, 98%), $Zn(CH_3COO)_2$ (Aldrich, 99.99%), and $Mn(NO_3)_2$ (Aldrich, 97.0%) were of analytical grade and were used without further purification. In a typical synthesis, one of the two half-cells was filled with freshly prepared 0.01 M Na_2S solution, that had been adjusted to a pH of 6.5~6.6 using 1 M HCl (Table S1) in order to inhibit formation of either $Zn(OH)_2$ or ZnO impurities (Figure S2). The other half-cell was immersed with a mixture of $Zn(CH_3COO)_2$ and $Mn(NO_3)_2$ in solution. Herein, $Mn(NO_3)_2$ was selected as the Mn source, not only because of its superior solubility as compared with other analogous Mn^{2+} salts (such as the chloride or stearate analogues, as illustrative examples) but also due to its incorporation of a common nitrate 'spectator ion' which did not interfere with the anticipated formation of the desired

sulfide compounds. The latter half-cell was characterized by a 0.01 M Zn^{2+} concentration, coupled with either 0, 0.002 M, 0.004 M, 0.006 M, 0.008 M, or 0.01 M Mn^{2+} concentrations, depending on the corresponding 0%, 20%, 40%, 60%, 80%, or 100% initial targeted doping ratios, respectively, as compared with the base Zn^{2+} concentration.

When permitted to diffuse and co-precipitate under ambient conditions, the reaction between these two solutions enabled the formation of the desired ZnS: Mn^{2+} anisotropic 1D nanostructures. As implied, the relevant co-precipitation reactions were initiated, when aqueous precursors from the two half-cells were allowed to react with each other within the confines of spatially restricted membrane pore channels. The system was then left unperturbed and allowed to react for an incubation period of 4 h at room temperature.[56] After the 4 h of incubation time, the polycarbonate membrane was detached, sonicated for 2 min, and polished to remove superfluous, unwanted particles on the surface. It was then thoroughly washed with distilled water, prior to its dissolution and removal with dichloromethane. As-prepared Mn-doped ZnS NWs were then collected, isolated from solution by centrifugation, and ultimately cleaned by washing.

(b) Post-synthesis annealing

In order to enhance the dopant-induced Mn^{2+} emission of as-prepared Mn-doped ZnS NWs, a post synthesis annealing process was also applied.[57] Typically, as-prepared Mn-doped ZnS NWs were vacuum dried, and heated to 600°C under 0.1 MPa pressure for 4 h within an atmosphere consisting of 5% hydrogen and 95% argon.

2.1.2 CdSe QDs, AET-capped CdSe QDs, & Heterostructures created by coupling 1D ZnS: Mn^{2+} with AET-capped CdSe QDs.

Colloidal CdSe QDs were prepared using a modification of an existing literature protocol.[58] Briefly, 0.2 mmol (25.8 mg) of CdO and 0.8 mmol (0.2316 g) of stearic acid were de-gassed at room temperature, and then heated at 150°C under an Ar atmosphere in order to completely dissolve the

various precursors within a three-necked flask. Subsequently, 0.8 mL aliquots of trioctylphosphine oxide (TOPO) and hexadecylamine (HDA) weighing 3.88 g each were added to the flask, and the mixture was heated to 320°C. In parallel, in an air-sensitive glovebox environment, 0.2 mmol (160.8 mg) of Se was dissolved in tributylphosphine (TBP) in the presence of 4.2 mL (14.1 mmol) of dioctylamine (DOA). The Se solution was later injected into the hot Cd precursor solution at 320°C, and QD growth could be carried out at 270°C for 13 s. The resulting, greenish mixture was later allowed to cool to room temperature, and the product was ultimately washed with a solution of either MeOH or acetone in order to remove impurities, prior to further dissolution in hexane.

CdSe QDs were then subjected to a ligand exchange reaction in order to facilitate their capping with AET, a mediating linker specifically chosen to connect CdSe QDs with the ZnS: Mn^{2+} nanowires and thereby facilitate the creation of our intended heterostructures. In a typical experiment, 1.7 mmol (0.2 g) of AET ligand, dissolved in 2 mL of EtOH, was added dropwise to a suspension of as-prepared TOPO/HDA-capped CdSe QDs (0.08 mmol) in 4 mL of hexane with a reactant molar concentration ratio of [ligands]/[QDs] = 25, with stirring. The molar ratio of [ligands]/[QDs] chosen herein is consistent with other reports for the effective promulgation of efficient ligand exchange from long alkyl chains to short thiol ligands.[59]

Hence, under "dark" conditions, i.e. in the absence of illumination, individual mixtures of the AET-capped CdSe QDs were stirred for 30 min. Visual confirmation for the completion of the ligand exchange process occurred as the CdSe QDs residing in the non-polar hexane layer were transferred to and subsequently re-dissolved into the polar EtOH layer, with the organic hexane layer becoming correspondingly clear. These ligand-exchanged QDs were later collected by centrifugation, washed with both MeOH and EtOH, and finally re-dispersed in EtOH for further processing.

To create the desired heterostructures, AET-capped CdSe QDs were immobilized onto annealed 1D ZnS: Mn^{2+} nanostructures presumably and primarily through electrostatic interactions, in a manner analogous to that of previous reports of and our own group's relevant experience with attaching

CdSe QDs onto not only underlying carbon nanotubes but also various binary and ternary metal oxides, such as TiO_2, ZnO, $CaTiO_3$, $CePO_4$, $CaWO_4$, $CaMoO_4$-$CaWO_4$, as well as $LaPO_4$.[32, 36, 47, 60-69]

In a typical experiment in order to create heterostructures with a molar compositional ratio of [ZnS: Mn^{2+}]: [AET-capped CdSe QDs]) of 1: 1.5, 3 μmol (0.3 mg) of ZnS: Mn^{2+} in 1 mL of EtOH was added to 4.5 μmol (0.9 mg) of AET-capped CdSe QDs in 2 mL of EtOH. The resulting solution was then sonicated for 10 min and stirred in the 'dark' for 2 h, prior to further processing and characterization, in order to preserve the optical integrity of the CdSe QDs. The identical method was utilized to generate analogous heterostructures possessing a molar compositional ratio of [ZnS: Mn^{2+}]: [AET-capped CdSe QDs]) of 1: 3.

2.2. Characterization

Samples were initially structurally probed and chemically characterized using a number of different complementary methodologies, including powder X-ray diffraction (XRD), transmission electron microscopy (TEM), energy-dispersive X-ray spectroscopy (EDS), and high resolution TEM (HRTEM). Moreover, additional optical characterization experiments were performed using UV−visible spectroscopy, steady-state photo-luminescence (PL) spectroscopy, as well as time-resolved fluorescence lifetime spectroscopy.

X-ray diffraction. Crystallographic and purity information on as-prepared 1D Mn doped ZnS NWs were obtained using powder X-ray diffraction. To prepare the relevant samples for analysis, powders of the 1D nanomaterials were initially dispersed in ethanol and then fully dried onto the surface of a zero-background holder (Si, MTI Corp.). Diffraction patterns were collected using a Rigaku Miniflex diffractometer, operating in the Bragg configuration using Cu Ka radiation (1.54 Å) with a typical scan range from 20 to 90° and using a scan rate of 10°/min.

Electron microscopy. A set of representative TEM images were acquired at an accelerating voltage of 120 kV on a JEOL JEM-1400 instrument, equipped with energy-dispersive X-ray

spectroscopy (EDS) elemental mapping capabilities as well as at 80 kV on a Technai12 BioTwinG2 TEM instrument. HRTEM images coupled with selected area electron diffraction (SAED) patterns were analyzed using both JEOL 2100 and JEOL 3000 microscopes, set at an accelerating voltage of 300 kV. Specimens for all of these microscopy experiments were initially prepared for analysis by dispersing the as-prepared products in ethanol and then drop-casting two aliquots of that solution onto lacey carbon film-coated 300 mesh Cu grids for both TEM and HRTEM analyses.

FT-IR measurements: FT-IR analysis was conducted in an effort to characterize the nature of the chemical bonding between the ZnS NWs and the CdSe QDs. In other words, we were looking to confirm the presence of aminoethanethiol. We used a ThermoNicolet 670 NEXUS instrument, equipped with a Smart Orbit diamond ATR accessory, a KBr beam splitter, and a DTGS KBr detector to amass the relevant FT-IR spectra. Data were collected by depositing a concentrated ethanolic solution of the sample onto the surface of a ZnSe crystal and subsequently applying reproducible pressure on the immobilized drop. Measurements were acquired over the wavelength range of 500-4000 cm^{-1} using the OMNIC software for 64 scans. The instrument maintained a spatial resolution of 4 cm^{-1}, operating in the transmittance mode. Baselines of acquired spectra were automatically accounted for, during processing of our sample data. Final images (Figure S5) were plotted using the Origin 8.0 software over a wavelength range of 500 to 4000 cm^{-1}.

UV-visible and fluorescence spectroscopy. UV-visible spectra were collected at high resolution using a Thermo Spectronics UV1 spectrometer in order to analyze the contents of the quartz cells, possessing a 10 mm path length. Spectra were obtained for AET-capped CdSe QDs, 1D ZnS: Mn^{2+}, as well as the corresponding heterostructures, respectively. Samples for PL spectra were dispersed in EtOH for AET-capped CdSe QDs, 1D ZnS: Mn^{2+} host materials, as well as ZnS: Mn^{2+} - AET-capped CdSe QD heterostructures with normalized concentrations.

Fluorescence data were then collected at room temperature using a FluoroMax-4 spectrofluorimeter (Jobin Yvon) and an ISS PC1 photon counting spectrofluorimeter (ISS Inc.,

Champagne, IL). In order to simultaneously excite all of the components, excitation wavelengths of 350 nm, as per the implications of our UV-visible spectral results (Figure 6), were applied. The corresponding fluorescence lifetimes acquired for AET-capped CdSe QDs, ZnS: Mn^{2+} hosts, and the associated heterostructures, respectively, were measured with a FluoroMax-4 spectrofluorimeter. This instrumentation was equipped with an IBH NanoLED, emitting at 388 nm as an excitation source, and a NanoLED controller module, i.e. Fluorohub (Jobin Yvon), operating at 1 MHz. The decay data analysis was completed using the DAS6 software (Horiba Jobin Yvon IBH).

3. Results and Discussion

3.1. Structural Characterization of as-prepared and annealed ZnS: Mn^{2+} Nanowires

Six ZnS-based NW samples possessing different initial Mn^{2+} doping amounts (ranging from 0% to 100%) were generated by utilizing the synthesis method, described earlier. In the following discussion, we focus on the '100% doping ratio' sample as a representative and illustrative example of the type of analysis we undertook and data we analyzed for all of the samples herein. The degree of crystallinity of these 1D ZnS: Mn^{2+} NWs, which had been prepared by an ambient U-tube template-mediated, solution-based synthesis method using templates with pore diameters of 200 nm, was initially characterized using X-ray diffraction (XRD).

The XRD patterns suggested that these as-synthesized (and non-annealed) NWs could be uniquely ascribed to a cubic sphalerite structure with major peaks located at 28.5°, 47.5°, and 56.2°, corresponding to the (111), (220), and (311) crystalline planes, respectively, a finding which agreed reasonably well with the reference JCPDS #05-0566 standard pattern (Figure 1A). In addition, the constituent crystallite size, as calculated by the Debye-Scherrer equation, was measured to be 3.0 nm for the as-prepared 1D ZnS: Mn^{2+} nanostructures, synthesized via the 200 nm pore diameter template channels.

The size, morphology, and crystallinity of our as-synthesized NWs have been subsequently investigated using TEM, HRTEM, and SAED. Representative TEM images of ZnS: Mn^{2+} NWs prepared with the use of 200 nm average diameter templates are shown in Figure 2A and B, and these data suggest measured diameters and lengths of 241 ± 30 nm and 2~3 μm, respectively, for our as-prepared nanowires.

HRTEM measurements on as-prepared nanowires (Figure 2C) further confirmed the presence of the cubic crystal structure of our as-prepared nanostructures with an indexed *d*-spacing of 0.317 nm, corresponding to the (111) plane of the zinc blende structure. Moreover, the SAED patterns (Figure 2D) were consistent with the XRD results, as the ring patterns could be reasonably assigned to signatures of the (111), (220), and (311) planes of cubic phase ZnS, respectively. Additionally, the diffuse and amorphous nature of these ring patterns could be ascribed to the overall polycrystalline nature of as-prepared ZnS: Mn^{2+} NWs.

In order to enhance the Mn^{2+} emission within as-prepared 1D ZnS: Mn^{2+}nanowires, a post-synthesis annealing approach, inspired by previous studies, was used in this work.[70] Specifically, it is known that the luminescence signal of doped Mn^{2+} is low, when the intrinsic crystallinity of the underlying ZnS host lattice is poor,[57] an observation attributable not only to the incomplete incorporation of Mn^{2+} within the ZnS crystal lattice but also to the spatial localization of Mn^{2+} primarily near the ZnS crystalline surfaces, lattice boundaries, and defect sites. As such, through the mediation of thermal treatments, such as annealing, the degree of crystallinity and average size of individual crystallites within the ZnS host can be increased.

From an optical perspective, the photophysical behavior of these annealed NWs is considerably improved upon, as greater ZnS crystallinity allows for increasing amounts of Mn^{2+} to be incorporated, and by extension, a stronger Mn^{2+} emission signal. In addition, it should be noted that the annealing process was conducted in a reducing gas atmosphere to prevent the formation of any potentially

deleterious oxidized species which might have led to unfavorable structural and photophysical complications.

Indeed, it has been predicted that a temperature-induced phase transition coupled with stoichiometrically undesirable oxygen incorporation can occur at temperatures higher than 500°C in O_2-rich environments.[70] Nevertheless, to enhance the crystallinity of our as-prepared ZnS nanowires, higher temperatures need to be achieved. Hence, herein, we used an atmosphere of 5% H_2 in 95% argon inert atmosphere to anneal the initial ZnS: Mn^{2+} nanostructures at a temperature of 600°C. A comparison of the XRD patterns of samples of as-prepared ZnS: Mn^{2+} NWs (100% Mn^{2+}) before annealing (Figure 1A) versus identical samples that had been annealed at 600°C for 4 h (Figure 1B) was consistent with a significant increase in the discrete crystallite size from 3.0 nm to 19.9 nm, i.e. corresponding to an increase of approximately 6 times in size after the annealing process, as estimated by the Debye-Scherrer equation. The cubic zinc blende phase of the underlying ZnS NWs was maintained, even after annealing at 600°C. However, we also observed the emergence of the würtzite phase of ZnS, suggestive of a phase transformation from the cubic to the hexagonal phase. Based upon the profile fitting generated using the Match! program, we computed the approximate compositional ratio between these two phases to be 60% zinc blende versus 40% würtzite phase.

As experimental validation for our annealing process, we note that in the PL emission spectra (Figure S3) of our ZnS: Mn^{2+} NWs, annealed at 600°C for 4 h, a strong Mn^{2+} emission was noted at ~580 nm (2.14 eV), whereas an analogous, as-prepared, and unannealed sample failed to demonstrate any emission of Mn^{2+} whatsoever. Moreover, we also observed a simultaneous reduction in the ZnS defect-related emission at wavelengths from 400 nm (3.1 eV) to 500 nm (2.48 eV) coupled with a corresponding increase in the Mn^{2+} emission within the annealed NWs. It is likely that the larger average crystal size (i.e. 19.9 nm) of the annealed sample, coupled with its improved structural integrity and lessening of intrinsic defects, played a role in these optical improvements.

To confirm these assertions, the morphological and structural properties of annealed 1D ZnS: Mn^{2+} NWs were probed using TEM, HRTEM, as well as SAED measurements. We note that the overall structural characteristics of these NWs, in terms of their 1D anisotropic motif and inherent dimensions, were found to have been preserved and maintained, even after annealing (Figure 3A and B). However, we found that the surface texture of these NWs appears to have coarsened after thermal treatment. Specifically, by contrast with their 'smoother' pre-heated textures (Figure 2A and B), the formation of a roughened surface on these annealed NWs was likely the result of the fusing, amalgamation, and re-orientation of crystalline domains during the annealing step. In addition, the HRTEM results and the SAED pattern also confirmed the presence of the expected cubic phase and a partial hexagonal phase as well as a perceptible improvement in the crystallinity of the annealed ZnS: Mn^{2+}, denoting findings corroborated by the presence of larger and more continuous crystalline domains as well as of well-aligned lattice orientations (Figure 3C and D).

As a key matter worth noting, we have observed that the amount of Mn^{2+} that was doped into the underlying ZnS host was ostensibly controlled by careful addition of the Mn^{2+} precursor coupled with meticulous manipulation of the relative Mn^{2+}/Zn^{2+} concentration ratio during the synthesis process. Nevertheless, our EDS data imply that our actual ZnS: Mn^{2+} NWs gave rise to much lower atomic Mn^{2+}/Zn^{2+} ratios in the range of 0.45% to 2.22% (Figure S4). The finding that the experimental ratio of Mn^{2+}/Zn^{2+} within our as-synthesized ZnS: Mn^{2+} nanowires was significantly smaller than what was primarily anticipated, based on the notably larger precursor concentrations used (20% to 100% ratios of Mn^{2+} to Zn^{2+}), can be possibly attributed to the considerably higher solubility product value (K_{sp}) of MnS (1.4×10^{-15}) as compared with that of the underlying ZnS (1.2×10^{-23}) matrix.[71] That is, it is likely that this substantial difference in the ease with which MnS and ZnS precipitate and subsequently form may have contributed to issues, associated with the full incorporation of dopant Mn^{2+} ions within the ZnS lattice.

Nonetheless, we have been able to empirically correlate the actual Mn^{2+} doping within our samples with increasing initial precursor concentrations of Mn^{2+}. Moreover, we should also note that whatever actual amount of Mn^{2+} ions end up becoming immobilized within the ZnS host, these cations are likely to be spatially, uniformly, and homogeneously distributed. In effect, our EDS data corroborate a relatively uniform signal intensity of Mn^{2+} within the corresponding nanostructures, regardless of the initial Mn^{2+} concentration (Figure S4).

3.2. Structural Characterization of ZnS: Mn^{2+} NW – AET-capped CdSe QD Heterostructures

Nanoscale heterostructures have been subsequently assembled by using 1D ZnS: Mn^{2+} as the underlying host matrix onto which AET-capped CdSe QDs were immobilized, after sonication and magnetic stirring. The morphology and uniformity of QD attachment were probed by using TEM, EDS, HRTEM, as well as SAED analysis.

The presence of attached and immobilized CdSe QDs along the outermost external surfaces of the ZnS: Mn^{2+} NWs can be visualized and verified, according to standard TEM data (Figure 4A and B). However, conventional TEM may not necessarily be capable of differentiating between the possible physical aggregation of QDs on the surfaces of the host NWs versus the presence of many discrete QDs. Moreover, the relatively poor contrast between the smaller-sized CdSe QDs versus the external surfaces of the ZnS: Mn^{2+} nanowires makes it difficult to both qualitatively and quantitatively assess the extent of QD localization onto the underlying 1D ZnS: Mn^{2+} motifs. Hence, we used EDS mapping, in addition to HRTEM studies, to complete our analysis.

To gain insights into the location and distribution of the elemental chemical composition in our composites, we acquired EDS data, which confirmed the expected presence of CdSe QDs within our as-prepared heterostructures. In particular, scanning transmission electron microscopy (STEM) images and corresponding elemental maps of representative ZnS: Mn^{2+} – AET-capped CdSe heterostructures are highlighted in Figure 5. These data provide evidence pertaining to the spatial distributions of the

various constituent elements of not only Zn, S, and Mn but also Cd and Se, which denote the elemental signatures of both the doped metal sulfide hosts and QDs, respectively.

Significantly, although there was the presence of some minor aggregation, we found that the Cd and Se signals associated with immobilized CdSe essentially overlapped relatively homogeneously in terms of spatial distribution with the analogous Zn, S, and Mn signatures connected to the Mn-doped ZnS NW hosts. Specifically, the locations of the Cd *L*-edge and the Se *K*-edge signals coincided reasonably well with those of the Zn *K*-edge, the S *L*-edge, and the M *K*-edge data (Figure 5), consistent with a picture in which the CdSe QDs were anchored onto and evenly distributed throughout the external surfaces of 1D ZnS: Mn^{2+} nanowire-based architectures in a uniform manner.

Moreover, the interface between the underlying ZnS host and CdSe QDs was further examined using HRTEM. Specifically, the lattice planes that could be specifically attributed to the two distinctive constituent components measured 0.317 and 0.372 nm, which were in good agreement with the expected *d*-spacings for the cubic zinc blende (111) plane and the hexagonal (100) plane of ZnS: Mn^{2+} NWs and CdSe QDs, respectively, within our as-prepared heterostructures (Figure 4C). The diffuse ring-like SAED patterns obtained on the surfaces of our heterostructures (Figure 4D) were consistent with their overall polycrystalline nature. Nonetheless, as is evident from our analysis, we were able to ascertain that certain ring patterns could be assigned to the expected (100) and (002) lattice planes of a hexagonal CdSe crystal structure, whereas additional ring patterns could be ascribed to the (111), (220), and (311) lattice planes, respectively, of cubic ZnS: Mn^{2+} nanocrystals. Hence, according to our cumulative data, it is likely that we were able to successfully achieve the formation of as-prepared heterostructures, comprised of ZnS: Mn^{2+} NW coupled with AET-capped CdSe QDs.

In terms of confirming the nature of the chemical bonding between the constituent 1D ZnS and 0D CdSe QDs within our heterostructures, FT-IR spectra were acquired with the data, as shown in Figure S5. Specifically, we collected FT-IR spectra of 1D ZnS: Mn^{2+} NWs, AET-capped CdSe QDs, and 1D ZnS: Mn^{2+} NW – AET-capped CdSe QD heterostructures, respectively. For the latter two QD-

derived materials, peaks located near 3200-3300 cm^{-1} and 1575 cm^{-1} can be attributed to N-H stretching vibrational and NH_2 scissoring modes, which are likely indicative of the existence of amino groups. Moreover, additional distinctive peaks positioned at 2918 cm^{-1}, 1370 cm^{-1}, and 1033 cm^{-1} can be reasonably ascribed to C-H stretching, C-N stretching, and C-S stretching modes, respectively, of the amine ligand molecules bound onto QDs, a finding consistent with the expected formation of AET-capped CdSe QDs. The peak near 2852 cm^{-1} likely represents the S-H stretching mode, which is associated with the thiol group of the AET linker molecule, and its presence confirms the formation of a chemical bond between the ZnS: Mn^{2+} NWs and the adjoining CdSe QDs within the context of a heterostructure motif. Other notable peaks positioned near 1066 cm^{-1} and 783 cm^{-1} can likely be assigned to the vibrational modes of ZnS. Hence, these cumulative set of spectroscopic data confirmed the presence of heterostructure formation, as expected.[36, 72]

3.3. Optical Characterization of as-prepared 1D ZnS: Mn^{2+} and ZnS: Mn^{2+} NW - AET-capped CdSe QD Heterostructures

3.3.1. Absorption.

UV−visible extinction spectra of all samples, i.e. (a) constituent 1D ZnS: Mn^{2+} (i.e. actual dopant level of 1.51%) NWs, (b) 'free', unassociated AET-capped CdSe QDs, as well as the corresponding (c) ZnS: Mn^{2+} - AET-capped CdSe QD heterostructures, were obtained. The spectra of samples (Figure 6) consisting of unbound AET-capped CdSe QDs exhibited well pronounced and defined peaks at ~500 nm, consistent with the excitonic absorption expected for QDs of this size (i.e. 2.3 nm), whereas annealed ZnS: Mn^{2+} NWs evinced a much wider adsorption feature, spanning wavelengths from 300 to 700 nm. According to previous work,[73] this broadening of the adsorption band could be attributed to the existence of a large amount of lattice vacancies and defects, which might account for the relatively strong defect-related ZnS emission we have observed.

In terms of the corresponding heterostructure, UV-visible spectra suggested and were consistent with the presence of AET-capped CdSe QDs immobilized on the external surfaces of the ZnS: Mn^{2+} NWs. Indeed, the resulting extinction curve possessed features that could be construed to be associated with both 0D QDs and the 1D host. Specifically, the first exciton feature (arrow in Figure 6) of AET-capped CdSe QDs, appearing at ~500 nm (i.e. 2.48 eV), was present in the extinction spectra of the resulting heterostructure at the same absorption wavelength. Moreover, the spectral broadening observed with annealed 1D ZnS: Mn^{2+} NWs was also present in that of the corresponding heterostructure, reflecting the profile of the 1D wires in that area. Because of the flattened spectrum associated with the annealed 1D ZnS: Mn^{2+} NWs, the presence of AET-capped CdSe QD immobilized onto the 1D NW surface cannot be conclusively proven using the data from the UV-visible spectrum only. Therefore, further PL optical measurements needed to be carried out.

3.3.2. Steady-State PL on annealed 1D ZnS: Mn NWs.

As a means of understanding and optimizing our photophysical data, we initially correlated the various Mn^{2+} doping ratios employed with the resulting Mn^{2+} emission intensities in an effort to select for the most optically active host components for the desired heterostructure formation with CdSe QDs. As such, we analyzed the photoluminescence (PL) behavior of annealed 1D ZnS: Mn^{2+} with different Mn^{2+} doping ratios at an excitation wavelength of 350 nm (~3.54 eV). The PL emission spectra of these samples exhibited the following trends.

The PL emission profile of ZnS: Mn^{2+} (regardless of Mn^{2+} dopant concentration) consisted of a broad ZnS defect-related emission shoulder located between 400 nm to 500 nm as well as a sharper feature situated at 580 nm (~2.14 eV) and associated with the $^4T_1$ to $^6A_1$ transition of Mn^{2+} (Figure S6). As compared with the typical emission signal associated with ZnS nanocrystals, the 1D motif of ZnS: Mn^{2+} possessed a slightly broader but comparable peak for ZnS defect-related emission. This observation is suggestive of the idea that the ZnS emission is defect-related and that it is influenced, to

a large extent, by the degree of crystallinity of the underlying host material itself.[74-75] Moreover, based upon prior work,[76] we can assign the individual substructures within our ZnS defect-related emission profile at wavelengths of 410 nm (i.e. 3.02 eV) and 432 nm (i.e. 2.87 eV) to interstitial state transitions in general, and more specifically to interstitial sulfur lattice defect (I_S) emission and interstitial zinc lattice defect (I_{Zn}) emission, respectively. Furthermore, peaks at 449 nm (i.e. 2.76 eV) and at 465 nm (i.e. 2.67 eV) can be ascribed to vacancy-induced transitions, associated with sulfur vacancy emission (V_S) and zinc vacancy (V_{Zn}) emission, in that order.[77]

Predictably, we detected a variation in the intensities of the Mn^{2+} intrinsic emission at 580 nm (i.e. ~2.14 eV) as a function of dopant Mn^{2+} concentration (Figure S6). Specifically, the intensity of the corresponding emission was found to have enhanced with actual Mn^{2+} doping ratios increasing from 0.45% to 2.22%, an observation which likely resulted from a corresponding rise in the amount of efficiently incorporated Mn^{2+} dopant ions. We note that we did not attempt to use higher doping ratios above 100% so as to avoid the possible formation of an MnS impurity, which might have been created, based upon the relatively low solubility product values of MnS and ZnS.

3.3.3. Steady-State PL on 1D ZnS: Mn^{2+} NWs - AET-capped CdSe QD heterostructures

Interestingly, the optical behavior of the corresponding ZnS: Mn^{2+} - AET-capped CdSe QD heterostructures revealed the impact of QD attachment. We observed a noticeable quenching effect not only on the defect-related emission of ZnS in the 400 to 500 nm wavelength region but also on the intrinsic emission of Mn^{2+}, located at 580 nm (i.e. ~2.14 eV), by comparing the black and red curves (Figure 7A). Specifically, the PL emission intensity of the 1D Mn^{2+} doped ZnS host (2.22%, Mn^{2+}) within ZnS: Mn^{2+} - AET-capped CdSe QD heterostructures, prepared with a molar ratio ([ZnS: Mn^{2+}]: [AET-capped CdSe QDs]) of 1: 1.5, yielded quenching and reduction of both the ZnS defect-related (400 - 500 nm) as well as the Mn^{2+} intrinsic emission (580 nm, ~2.14 eV).

Quantitatively, the ZnS defect-related emission diminished by a factor of 44.8%, as calculated from alterations in the 410 nm peak intensity by comparing its evolution from that noted within ZnS: Mn^{2+} NW curve to that observed in the corresponding heterostructure curve. For the analogous Mn^{2+} intrinsic emission, we observed a reduction of 35.1%, as computed from changes in the 580 nm peak intensity by monitoring its progression from that seen within 'free', well-dispersed 1D ZnS: Mn^{2+} nanostructures to that found with the corresponding curve of as-prepared heterostructures. The proposed origins of the observed quenching behavior within these heterostructures could be ascribed to not only (a) the combined effects of hole transfer and energy transfer from ZnS defect sites to QDs, thereby impacting the observed ZnS defect-related emission, but also (b) the presence of hole transfer from the $^6A_1$ state of Mn^{2+} to the valence band (VB) of QDs, thereby accounting for the decrease in the observed Mn^{2+} emission.

The PL emission variation in the signal profiles of both free (i.e. unbound) as well as immobilized CdSe QDs (Figure 7B) was also studied. Specifically, the emission of attached CdSe QDs within the corresponding heterostructures was also quenched. We attribute this observation to an electron transfer from the conduction band of immobilized CdSe QDs themselves to the analogous CB of ZnS, due in part to the unique band gap alignment of nanoscale CdSe QDs with respect to that of ZnS. By contrast, energy transfer from the ZnS host to the bound QDs, due to a favorable superimposition and overlap of the absorption wavelengths of QDs (350~500 nm) with the defect-related emission wavelengths (400~500 nm) of the underlying ZnS host, could have led to an increase in the CdSe QD peak emission within the heterostructure (Figure 11). Herein, there is a competition between the contending energy transfer and charge transfer processes within this heterostructure. Because we noted a decrease in the overall emission intensity, we propose that charge transfer likely was more dominant than energy transfer. A detailed explanation and rationale for all of the charge and energy transfer processes will be presented in Section 3.4.

In addition, as a function of the relative molar concentrations (i.e. from 1: 1.5 to 1: 3 of ZnS: Mn^{2+} wires to bound CdSe quantum dots) of both constituent 0D and 1D components within our as-prepared ZnS: Mn^{2+} - AET-capped CdSe QD heterostructures, we detected a more significant quenching of both ZnS defect-related and Mn^{2+} intrinsic emission intensities (Figure 8) in the presence of greater CdSe QD concentrations. Specifically, by comparing the intensities of ZnS and Mn^{2+} emission peaks before and after the addition of a 3-fold molar excess of CdSe QDs relative to the amount of the underlying host material (Table 1), we found that the amount of the observed quenching increased for both the ZnS emission (Q_{ZnS}) and the Mn^{2+} emission (Q_{Mn}) to be as much as 58.4 % and 44.2% of the initial values, respectively, corresponding to factors of 1.30 and 1.26 greater than analogous data collected when the molar excess of CdSe QDs with respect to the host material content was merely 1.5 (Table 1).

Nevertheless, we also perceived comparable attenuation behaviors of CdSe QD emission within both heterostructures composed of molar ratios of ([ZnS: Mn^{2+}]: [AET-capped CdSe QDs]) of '1: 1.5' and '1: 3', respectively. To account for this observation, we note that a larger quantity of QDs (i.e. a [ZnS: Mn^{2+}]: [AET-capped CdSe QDs] molar ratio of 1: 3) on the host surface simultaneously promotes not only energy and hole transfer from the ZnS lattice to the QDs but also charge (specifically, electron) transfer from the CB of the QDs to that of ZnS. As a result, these two competing processes 'cancelled' each other out to some extent, and overall, led to a net reduction in the emission intensity of this composite material (incorporating a greater QD content) as compared with that of the analogous heterostructure, characterized by a lower molar ratio of QDs, i.e. the sample possessing a [ZnS: Mn^{2+}]: [AET-capped CdSe QDs] molar ratio of 1: 1.5.

We can attribute this QD concentration-dependent phenomenon to the substantially greater coverage of QDs on the underlying hosts with the use of larger molar excesses of QDs, as leading to an increased interfacial surface area for interaction between the 1D ZnS: Mn^{2+} and the 0D QDs, thereby enabling a more efficient energy and charge transfer process.[78] Moreover, the greater amount of

quenching noted with the ZnS emission as opposed to the Mn^{2+} emission (Table 1) is consistent with the idea of simultaneous energy and charge transfer occurring from the ZnS:Mn^{2+} host itself to the attached QDs. Therefore, by rationally adjusting the molar concentrations of these two constituent components within the heterostructure, an architectural motif possessing tunable multi-emissive properties can in theory be readily produced.

To further probe the interaction between immobilized CdSe QDs and ZnS: Mn^{2+}, the emission decay behavior of ZnS: Mn^{2+} - AET-capped CdSe heterostructures was analyzed with the use of a 388 nm laser pulse excitation source. The results with fitted data were independently collected on all three emission bands in question, namely those derived from ZnS, Mn^{2+}, and CdSe, respectively (Figure 9). Because the distribution and convolution of recombination rate constants associated with our complex heterostructured architecture likely influenced the resulting decay kinetics, the intensity decay performance of all three emission bands was examined and modeled, according to tri-exponential decay kinetics (Equation 1),[79-80] in order to determine the corresponding individual emission lifetimes (τ_i). Subsequently, these values were used to further estimate the average lifetimes (τ_{av}) of the respective emission decays considered (Equation 2).[79, 81]

$$F(t) = a_1 \exp\left(\frac{t}{\tau_1}\right) + a_2 \exp\left(\frac{t}{\tau_2}\right) + a_3 \exp\left(\frac{t}{\tau_3}\right) \quad (1)$$

$$\tau_{av} = \frac{\sum a_i \tau_i^2}{\sum a_i \tau_i} \quad (2)$$

However, the trends for all three emissions observed were different, depending on the three emission regions analyzed. Importantly, these behaviors could not be solely attributed to the quenching induced by the presence of the 0D QDs within the composite. Specifically, the average lifetime (τ_{av}) of the ZnS defect-related emission (centered on the V_{zn} emission located at 465 nm) remained relatively steady from 0.95 ns in as-prepared samples to 0.97 ns and finally attained a value of 0.53 ns, as the amount of CdSe QDs was systematically increased from a molar excess of 1.5 to 3 within the corresponding heterostructures (Figure 9A). By contrast, the average lifetimes (τ_{av}) of the Mn^{2+}

emission perceptibly increased with increasing concentrations of CdSe QDs within the resulting heterostructures, i.e. 4.44 ns for Mn^{2+} emission in as-prepared NWs versus 9.08 ns and ultimately 12.75 ns, as the molar ratio of CdSe QDs relative to that of ZnS: Mn^{2+} was correspondingly raised from 1.5: 1 to 3: 1 (Figure 9B). We should note that the average lifetimes (τ_{av}) of free as well as of bound AET-capped CdSe QDs were noted to be 7.28 ns and 5.26 ns, respectively. Indeed, the observed trends in the lifetime data associated with the three emission regions do not necessarily corroborate the corresponding results from the PL emission spectra (Figure 9C), but nonetheless, these data can be explained with further analysis, based upon relative energy level alignments (Section 3.4).

In general, in a heterostructure, a shorter observed lifetime of a particular material component is normally indicative of charge transfer to an adjoining constituent unit. With respect to the ZnS defect-related emission (465 nm, Figure 7A) region, we found that the lifetime change is relatively small, i.e. from 0.95, 0.97, to 0.53 ns over the range of heterostructures studied. Yet, we perceived a considerable quenching phenomenon. This juxtaposition in ZnS of a significant quenching effect coupled with a relatively minor alteration in the lifetime is consistent with competing and simultaneous charge transfer processes occurring not only from (i) the conduction band of the CdSe QDs to that of ZnS: Mn NWs but also from (ii) the CB of the ZnS: Mn NWs to that of the Mn^{2+} dopant itself. Hence, in this scenario, the Mn^{2+} emission possesses a longer lifetime after CdSe QD attachment, because of a predominant net charge transfer process taking place from the conduction band of the QD to the CB of the Mn^{2+} dopant, via the mediation of the CB of the ZnS: Mn NWs. Finally, the observation of a shorter lifetime of bound CdSe QDs suggests the existence of charge transfer from the CB of the immobilized CdSe QDs to the corresponding CB of the underlying ZnS: Mn NWs.

To summarize, (i) the obvious excitonic emission quenching and relatively unchanged lifetimes of self-activated ZnS, (ii) the apparent emission quenching and longer lifetimes of Mn^{2+} dopant-related emissions, coupled with (iii) the decreased emission intensities and lower decay times of CdSe QDs within the ZnS: Mn^{2+} - AET-capped CdSe QD nanoscale heterostructures are collectively indicative of

the reasonable hypothesis that photo-generated charge and/or energy transfer represents a significant relaxation pathway within these 1D-0D composite architectures. The directionality and extent of the observed charge transfer and energy transfer likely affect the magnitude and the corresponding variation in the observed emission intensity and decay (lifetime) profile. These observations will be discussed in detail in the next section.

3.4. Data interpretation based on energy level alignments.

To better understand all of these experimental observations, the respective energy level alignments of ZnS: Mn^{2+}, CdSe QDs, as well as of the connective AET ligand itself need to be considered. Figure 10 highlights the schematic diagram of the energy levels associated with all of these species, i.e. ZnS: Mn^{2+}, CdSe QDs, and AET, respectively. On the basis of previous studies, it is reasonable to assert that the valence band (VB) of the ZnS host (i.e., −7.2 eV relative to the vacuum level)[77] is located below the corresponding VB of as-prepared 2.3 nm average diameter CdSe QDs (i.e., −5.57 eV relative to the vacuum level, denoting a calculated value, based upon a prior report).[82]

This scenario should therefore be conducive towards inducing luminescence quenching of ZnS emission within ZnS: Mn^{2+} NW-AET-capped CdSe QD heterostructures as a result of hole transfer occurring from the ZnS host to the attached CdSe QDs, when the ZnS: Mn^{2+} motifs are optically excited, in particular. As previously mentioned, in addition to hole transfer, the presence of energy transfer from the ZnS host to the bound CdSe QDs also contributes to the efficient quenching behavior of ZnS itself, an assertion which has been verified by (a) observing the relative positions of the relevant energy bandgaps of ZnS and 2.3 nm CdSe QDs (Figure 10), as well as by (b) overlaying the absorption spectrum of as-prepared QDs with the corresponding PL emission spectrum of the ZnS: Mn^{2+} host (Figure 11). Specifically, the ZnS defect-related emission peaks are coincidently located between the wavelengths of 400 nm to 500 nm, which is well within the absorption region of CdSe QDs. Therefore, energy transfer from the ZnS: Mn^{2+} host to the immobilized CdSe QDs is both viable and feasible.

In terms of the Mn^{2+} emission quenching, with respect to the band alignments, the $^6A_1$ state of Mn^{2+} (i.e., -6.2 eV relative to the vacuum level)[83] is located below the VB of the CdSe QDs (i.e., −5.57 eV relative to the vacuum level).[82] Hence, it is energetically favorable for holes to transfer from Mn^{2+} to the CdSe itself, which would consequently reduce the $^4T_1$ to $^6A_1$ recombination efficiency and thereby lead to a quenched Mn^{2+} emission intensity within the corresponding heterostructures. Moreover, since the emission of Mn^{2+} is located well beyond the absorption region of AET-capped CdSe QDs with little or no overlap (Figure 11) and because the energy bandwidth associated with the $^4T_1$ to $^6A_1$ transition of Mn^{2+} is significantly narrower than that of the relevant bandgap inherent to 2.3 nm average diameter QDs (Figure 10), energy transfer is less likely to occur from the Mn^{2+} emission center to the CdSe QDs. Hence, by contrast with Mn^{2+} dopant-induced emission which is dominated by charge transfer, the combination of both charge and energy transfer effects likely induces quenching of the ZnS self-activated emission profile.

Moreover, the diminished quantum emission intensity of CdSe QDs within the heterostructures can also be explained as a product of energy transfer from the ZnS: Mn^{2+} host to the QDs competing with electron transfer processes occurring in the opposite direction. Specifically, the non-radiative flow of high-energy UV-induced electrons from CdSe QDs to the underlying ZnS host is energetically favored, since the CB of as-prepared 2.3 nm average diameter CdSe QDs (i.e. -2.43 eV relative to the vacuum level, denoting a calculated value based upon a previous report)[82] is located above the analogous CB value (i.e. -3.52 eV relative to the vacuum level)[77] of ZnS: Mn^{2+}.

In terms of understanding the QD concentration effect with this model, we have already noted that interactions between 1D ZnS: Mn^{2+} and 0D CdSe QDs affect both the charge and energy transfer processes. Consequently, with additional CdSe QDs attached onto the surface of the underlying Mn-doped ZnS motif, we would expect not only (i) additional hole transfer from the $^6A_1$ state of Mn^{2+} to the VB of the CdSe, thereby resulting in a proportionally greater amount of Mn^{2+} emission quenching, but also (ii) an increased amount of energy transfer and hole transfer from the 1D ZnS: Mn^{2+} to the 0D

QDs competing with electron transfer from the QDs to the 1D ZnS: Mn^{2+} in the reverse direction. Based upon this energy alignment picture, we would reasonably predict that the net consequence of all of these simultaneously ongoing processes would likely be an enhanced PL intensity quenching in the behavior of heterostructures with progressively higher and increasing QD coverages, such as composites incorporating successively greater molar ratios of ([ZnS: Mn^{2+}]: [AET-capped CdSe QDs]) of '1: 1.5' onwards to '1: 3'. This is exactly what we have experimentally observed herein, as corroborated by the data in Table 1. .

3.5. Study of Chromaticity.

In order to further probe the optical properties and color range of our newly synthesized ZnS: Mn^{2+} NW - AET-capped CdSe QD heterostructures, we analyzed their potential multi-emissive range, spanning wavelengths from 400 nm to 700 nm, in order to investigate their possible use as a white light-emitting material for future light-emitting applications. In this regard, the chromaticity of as-prepared heterostructures has been systematically studied.

Specifically, based upon our PL emission spectra, data on the visible light emission behavior of our 1D-0D heterostructures were converted into their corresponding chromatic color coordinates, as highlighted in the Commission International de l'éclairage (CIE) chromaticity diagram. In so doing, the representative observed and defining color ranges, generated after integrating all colors emitted from the analyzed material, could be accurately measured in a quantitative manner. Initially, the optical profiles of as-synthesized AET-capped CdSe QDs, of ZnS: Mn^{2+} NWs (with an actual 2.22% Mn^{2+} dopant ratio), as well as of the resulting heterostructures characterized by a molar constituent component [ZnS: Mn^{2+} NW]: [AET-capped CdSe QD] ratio of 1: 1.5 were measured.

'Free', unbound AET-capped CdSe QDs and ZnS: Mn^{2+} NWs with an actual 2.22% Mn^{2+} dopant ratio (Figure 12A) yielded chromaticity coordinates of (0.35, 0.51) and (0.37, 0.34), respectively, corresponding to green and orange light emission, respectively. By contrast and very

interestingly, our corresponding 1D-0D heterostructures can be considered as white light-emitting candidates, as they gave rise to a chromaticity coordinate of (0.37, 0.39), a value well within the broad white light-emitting region (Figure 12 A and B) and close to the 'perfect' white light emission scenario, which is characterized by an analogous coordinate of (0.33, 0.33).

Additionally, the concentration effects of the various different nanoscale constituent components upon the white light color-emitting behavior of the corresponding heterostructures were also systematically examined. We found that increasing the QD content to a molar excess of 3 with respect to the host material content worsened the white light emitting performance of the resulting heterostructures. In fact, the observed emission profile included more green and yellow hues, likely emanating from the CdSe QD emission itself (Figure 12A).

On the other hand, the heterostructures did exhibit a degree of tunability in the 'white-color' region by tailoring the concentration of Mn^{2+} dopants within the ZnS lattice. For example, by simply decreasing the definitive Mn^{2+} dopant content from 2.22% to 1.51%, the color coordinate of the resulting heterostructure shifted from (0.37, 0.39) to (0.33, 0.38) with the shift localized within the generalized white-light emitting region (Figure 12B and S7). Furthermore, as the actual Mn^{2+} ratio in the host was reduced from 2.22% to 1.51%, the orange Mn^{2+} emission became weaker than the corresponding blue ZnS self-activated emission, thereby yielding a greater contribution of blue light emission to the corresponding emission spectrum of the associated heterostructures (Figure 8 and S7A). That is, as compared with the use of 2.22% Mn^{2+} dopants, a drop in the Mn^{2+} content to 1.51% directly led to a shift in the color coordinates towards the blue region in the CIE diagram (Figure 12B, S7B and Table S2). We should also note that with a 1.75% Mn^{2+} doping amount, we measured a color coordinate of (0.35, 0.38), which is situated between the values for the analogous 1.51% and 2.22% doping ratios. That is, with lower Mn^{2+} doping ratios, we consistently observed a shift in the color coordinates towards the blue region. Furthermore, with 1.19% and 0.45% doping ratios, we obtained color coordinates of (0.32, 0.35) and (0.29, 0.35), respectively. From our cumulative data, we have

demonstrated that the use of a 1.19% Mn^{2+} doping ratio ensures that we are closest to the 'perfect' white light emission scenario.

Moreover, the associated correlated color temperatures (CCT) were calculated based upon color coordinates and McCamy's third-order polynomial function equations[84] (i.e. Equations 3 and 4 below, wherein 'x_e' and 'y_e' designate epicenter coordinates of 0.3320 and 0.1858; 'a', 'b', 'c', and 'd' are constants of -449, 3525, -6823.3, and 5520.3; and 'x' and 'y' represent color coordinates of the corresponding samples).

$$n = (x - x_e)/(y - y_e) \qquad (3)$$

$$CCT = an^3 + bn^2 + cn + d \qquad (4)$$

These computations suggested that a heterostructure incorporating a real Mn^{2+} dopant ratio of 2.22% (i.e. yielding more yellow/red emission) exhibited a 'warmer-white' light emitting nature with a CCT of 4383 K, whereas analogues possessing a lower actual Mn^{2+} dopant ratio of 1.51% (i.e. giving rise to more blue emission) displayed a 'colder-white' light emitting property with a calculated CCT of 5676 K, as compared with a reference white CCT of 5460 K. The analogous CCT values for samples with 1.75%, 1.19%, and 0.45% Mn dopant ratios are 5234 K, 6286 K, and 7444 K, respectively. Moreover, we have been able to summarize and plot the data in a CIE chromaticity diagram for all of our heterostructures possessing different Mn^{2+} doping ratios with the amount of attached AET-capped CdSe QDs kept constant. In effect, we have found that by systematically decreasing the Mn^{2+} doping ratio, we could effectively shift (i) the observed color coordinates from the yellow to the blue region, and (ii) the corresponding CCT data from a 'warmer-white' to a 'colder-white' light emission.

Consequentially, by simply altering the inherent chemical composition of our 1D-0D heterostructures, we were able to demonstrate the precise optical tuning of our composite architectures from a 'warm-white' light emitter to a 'cold-white' light emitting material. Therefore, our chemically-induced ability to viably tailor the emission behavior between a 'cold-white' to a 'warm-white' hue of

our as-prepared heterostructures endows our novel motifs with significant potential to serve within the context of truly innovative architectures for versatile solid-state light applications.

4. Conclusions

In this study, for the first time, 1D Mn-doped ZnS were initially synthesized using an ambient, wet solution-based, template-assisted, U-tube-based method. In particular, the spatially confined channels of commercial polycarbonate-based templates possessing nominal pore sizes of 200 nm were used to generate doped 1D ZnS nanostructures with lengths of ~3 μm and average diameters of 241 ± 30 nm, respectively. These as-prepared 1D motifs were characterized by a pure cubic zinc-blende phase with an average crystallite size of around 3.0 nm.

The observed Mn^{2+} emission associated with the $^4T_1$ to $^6A_1$ transition of Mn^{2+} was significantly enhanced after an annealing treatment in a reducing atmosphere at 600°C for 4 h. In particular, in addition to an increase in overall crystallinity, the average crystallite sizes of annealed ZnS: Mn^{2+} nanowires were found to have increased to 19.9 nm, all of which considerably improved the observed Mn^{2+} emission, as there was likely to be more efficient incorporation of Mn^{2+} within these annealed samples. PL studies confirmed that the 1D ZnS: Mn^{2+} with an actual, optimized Mn^{2+} doping ratio of 2.22% appeared to yield the highest emission, while the use of a lower amount of doping led to a decreased Mn^{2+} emission intensity.

More importantly, our resulting 1D-0D heterostructures reported herein take advantage of the use of as-prepared 1D ZnS: Mn^{2+} as the host materials with their optical behavior emanating from dual emission from both self-activated and dopant-stimulated centers. By contrast, much of the prior literature has relied on the use of hosts, whose emission properties resulted solely from the presence of either external dopant species or the presence of intrinsic lattice defects. From a photophysical perspective, our as-prepared nanoscale ZnS: Mn^{2+} NW - AET-capped CdSe QD heterostructures were found to display PL quenching for both ZnS and Mn^{2+} emission bands as compared with unbound 1D

ZnS: Mn^{2+}, due to a photoexcited charge transfer process occurring from both ZnS and Mn^{2+} species to CdSe QDs as well as energy transfer from the ZnS host to the immobilized CdSe QDs. Similarly, there was a decreased emission intensity in the PL output profiles of CdSe QDs, incorporated within as-prepared heterostructures, as compared with free, unbound CdSe QD species.

This noticeable difference in the optical behavior between the 1D ZnS: Mn^{2+} hosts and the CdSe QDs can be explained based upon the relative energy level alignment between ZnS: Mn^{2+} and CdSe QDs. Specifically, the VB levels of ZnS and of the $^6A_1$ state of Mn^{2+} are situated at significantly lower energies than that of the corresponding HOMO levels of the connecting AET linkers as well as that of CdSe QDs, thereby promoting and facilitating hole transfer from ZnS and Mn^{2+} to the attached CdSe QDs through an intermediary AET linker agent. Potential energy transfer from the ZnS host to the immobilized CdSe QDs could be attributed to the existence of energy bandgaps of favorable magnitude and alignment as well as to the propitious overlap between the absorption and emission wavelength regions of the QDs and of ZnS, respectively.

We should note that the co-existence of competing processes, such as energy transfer from ZnS to CdSe coupled with electron transfer from the VB of CdSe to that of ZnS, resulted in a nuanced interpretation of the overall slightly decreased quantum emission observed within these heterostructures. Furthermore, we observed and correlated greater and more pronounced PL quenching of both ZnS defect-related emission and intrinsic Mn^{2+} emission related to 1D ZnS: Mn^{2+} within the corresponding heterostructures with increasing quantities of immobilized CdSe QDs, a likely consequence of an increased efficiency of interaction with the underlying ZnS host as a function of greater QD coverage.

In addition to the unique combination of charge and energy transfer phenomena described above, we noted that the particular tunable chromaticity emanating from the co-existence and manipulation of 3 independent emission band 'building blocks', corresponding to the constituent ZnS, the Mn^{2+} dopant, and the CdSe QD components within our heterostructures. Indeed, based upon a

quantitative study of integrated chromaticity color coordinates converted from corresponding PL emission spectra in addition to the calculation of correlated color temperature (CCT) measurements, estimated based upon McCamy's equation, our results highlight the white-color emitting nature of heterostructures fabricated using ZnS: Mn NWs (with an actual 2.22 % Mn^{2+} dopant) and AET-capped CdSe QDs with a 1: 1.5 molar ratio.

The estimated chromaticity coordinate of (0.37, 0.39) for our heterostructures closely correlates with the (0.33, 0.33) coordinate expected for a reference white color. Moreover, the chromaticity coordinate could be further tuned by tailoring either the sulfide host / QD ratio or the Mn^{2+} doping ratio. Significantly, we were able to engineer a shift from (0.29, 0.35) to (0.37, 0.39) within the overall white color region upon reducing the actual Mn^{2+} dopant ratio from 2.22% to 0.45%. Combined with the CCT results, we can conclude that the integrated emission band of our 1D-0D heterostructures can be tuned from a 'cold-white' hue (i.e. 7444 K) to a 'warm-white' tinge (i.e. 4383 K), simply by tailoring the dopant Mn^{2+} concentration.

Overall, the implication of creating novel tunable white light emitting ZnS: Mn -AET-capped CdSe QD heterostructures using a facile, reliable, and mainly ambient approach in this study not only opens up new, functional, and viable architectures for the feasible fabrication of white light-emitting semiconductors for potential applications on smart and multifunctional devices but also provides for an understanding and clear delineation of interface-mediated charge and energy transfer processes that impact upon their photophysical properties. As such, our system becomes substantively crucial as a model system for the design of multi-functional, simultaneously photo-luminescent and light emitting architectures with tunable emissive behavior.

Acknowledgements:

Research for all authors was supported by the U.S. Department of Energy, Basic Energy Sciences, Materials Sciences and Engineering Division. Experiments for this manuscript were

performed in part at the Center for Functional Nanomaterials located at Brookhaven National Laboratory, which is supported by the U.S. Department of Energy under Contract No. DE-SC-00112704. We thank Luyao Li for FT-IR data acquisition, associated with Figure S5.

References

[1] C. Feldmann, T. Justel, C. R. Ronda, P. J. Schmidt, *Adv. Funct. Mater.* **2003**, *13*, 511.

[2] S. Ye, F. Xiao, Y. X. Pan, Y. Y. Ma, Q. Y. Zhang, *Mater. Sci. Eng. R* **2010**, *71*, 1.

[3] M. M. Shang, C. X. Li, J. Lin, *Chem. Soc. Rev.* **2014**, *43*, 1372.

[4] S. K. Panda, S. G. Hickey, H. V. Demir, A. Eychmuller, *Angew. Chem.* **2011,** 123,4524; *Angew. Chem. Int. Edit.* **2011**, *50*, 4432.

[5] T. E. Rosson, S. M. Claiborne, J. R. McBride, B. S. Stratton, S. J. Rosenthal, *J. Am. Chem. Soc.* **2012**, *134*, 8006.

[6] M. Roushan, X. Zhang, J. Li, *Angew. Chem.* **2012**, *124*, 451; *Angew. Chem. Int. Edit.* **2012**, *51*, 436.

[7] C. H. Huang, P. J. Wu, J. F. Lee, T. M. Chen, *J. Mater. Chem.* **2011**, *21*, 10489.

[8] X. M. Liu, C. X. Li, Z. W. Quan, Z. Y. Cheng, J. Lin, *J. Phys. Chem. C* **2007**, *111*, 16601.

[9] Z. C. Wu, J. Liu, W. G. Hou, J. Xu, M. L. Gong, *J. Alloys Compd.* **2010**, *498*, 139.

[10] J. S. Kim, P. E. Jeon, Y. H. Park, J. C. Choi, H. L. Park, G. C. Kim, T. W. Kim, *Appl. Phys. Lett.* **2004**, *85*, 3696.

[11] M. M. Shang, G. G. Li, X. J. Kang, D. M. Yang, D. L. Geng, C. Peng, Z. Y. Cheng, H. Z. Lian, J. Lin, *Dalton Trans* **2012**, *41*, 5571.

[12] A. M. Jakob, T. A. Schmedake, *Chem. Mater.* **2006**, *18*, 3173.

[13] T. Ogi, Y. Kaihatsu, F. Iskandar, W. N. Wang, K. Okuyama, *Adv. Mater.* **2008**, *20*, 3235.

[14] C. M. Zhang, C. X. Li, J. Yang, Z. Y. Cheng, Z. Y. Hou, Y. Fan, J. Lin, *Langmuir* **2009**, *25*, 7078.

[15] C. K. Lin, Y. Luo, H. You, Z. Quan, J. Zhang, J. Fang, J. Lin, *Chem. Mater.* **2006**, *18*, 458.

[16] C. K. Lin, M. Yu, Z. Y. Cheng, C. M. Zhang, O. G. Meng, J. Lin, *Inorg. Chem.* **2008**, *47*, 49.

[17] S. Pramanik, S. Bhandari, S. Roy, A. Chattopadhyay, *J. Phys. Chem. Lett.* **2015**, *6*, 1270.

[18] Y. Q. Li, A. Rizzo, R. Cingolani, G. Gigli, *Microchim. Acta* **2007**, *159*, 207.

[19] W. Chen, L.-P. Xu, S. Chen, *J. Electroanal. Chem.* **2009**, *631*, 36.

[20] S. Kandoi, P. A. Ferrin, M. Mavrikakis, *Top. Catal.* **2010**, *53*, 384.

[21] S. Kuchibhatla, A. S. Karakoti, D. Bera, S. Seal, *Prog. Mater. Sci.* **2007**, *52*, 699.

[22] C. M. Lieber, *Solid State Commun.* **1998**, *107*, 607.

[23] L. Carrette, K. A. Fridrich, U. Stimming, *Chemphyschem* **2000**, *1*, 162.

[24] C. M. Lieber, Z. L. Wang, *MRS Bull.* **2011**, *32*, 99.

[25] M. Bruchez, M. Moronne, P. Gin, S. Weiss, A. P. Alivisatos, *Science* **1998**, *281*, 2013.

[26] W. A. Tisdale, K. J. Williams, B. A. Timp, D. J. Norris, E. S. Aydil, X.-Y. Zhu, *Science* **2010**,

328, 1543.

[27] R. I. Cukier, D. G. Nocera, *Annu. Rev. Phys. Chem.* **1998**, *49*, 337.

[28] L. Samuelson, M. T. Björk, K. Deppert, M. Larsson, B. J. Ohlsson, N. Panev, A. I. Persson, N. Sköld, C. Thelander, L. R. Wallenberg, *Phys. E* **2004**, *21*, 560.

[29] X. Peng, M. Y. Sfeir, F. Zhang, J. A. Misewich, S. S. Wong, *J. Phys. Chem. C* **2010**, *114*, 8766.

[30] X. Peng, A. C. Santulli, E. Sutter, S. S. Wong, *Chem. Sci.* **2012**, *3*, 1262.

[31] L. Wang, Y. R. Li, J. Li, S. Zou, E. A. Stach, K. J. Takeuchi, E. S. Takeuchi, A. C. Marschilok, S. S. Wong, *ECS J. Solid State Sci. Technol.* **2017**, *6*, M3122.

[32] J. Han, C. McBean, L. Wang, C. Jaye, H. Liu, D. A. Fischer, S. S. Wong, *J. Phys. Chem. C* **2015**, *119*, 3826.

[33] L. Wang, J. Han, B. Sundahl, S. Thornton, Y. Zhu, R. Zhou, C. Jaye, H. Liu, Z. Q. Li, G. T. Taylor, D. A. Fischer, J. Appenzeller, R. J. Harrison, S. S. Wong, *Nanoscale* **2016**, *8*, 15553.

[34] R. S. Selinsky, Q. Ding, M. S. Faber, J. C. Wright, S. Jin, *Chem. Soc. Rev.* **2013**, *42*, 2963.

[35] Y. Zhu, R. Zhou, L. Wang, S. S. Wong, J. Appenzeller, *ACS Energy Lett.* **2017**, *2*, 717.

[36] J. Han, L. Wang, S. S. Wong, *RSC Adv.* **2014**, *4*, 34963.

[37] J. Han, C. McBean, L. Wang, J. Hoy, C. Jaye, H. Liu, Z.-Q. Li, M. Y. Sfeir, D. A. Fischer, G. T. Taylor, J. A. Misewich, S. S. Wong, *Chem. Mater.* **2015**, *27*, 778.

[38] J. Han, L. Wang, S. S. Wong, *J. Phys. Chem. C* **2014**, *118*, 5671.

[39] P. L. McEuen, *Nature* **1999**, *393*, 15.

[40] S. Saito, *Science* **1997**, *278*, 77.

[41] E. Unger, G. S. Duesberg, M. Liebau, A. P. Graham, R. Seidel, F. Kreupl, W. Hoenlein, *Appl. Phys. A* **2003**, *77*, 735.

[42] S. Ravindran, C. S. Ozkan, *Nanotechnology* **2005**, *16*, 1130.

[43] L. Samuelson, *Mater. Today* **2003**, 22.

[44] Q. Jin, Y. Hu, Y. Sun, Y. Li, J. Huo, X. Zhao, *RSC Adv.* **2015**, *5*, 41555.

[45] M. Geszke, M. Murias, L. Balan, G. Medjahdi, J. Korczynski, M. Moritz, J. Lulek, R. Schneider, *Acta Biomater.* **2011**, *7*, 1327.

[46] H. Zhou, J. Chen, E. Sutter, M. Feygenson, M. C. Aronson, S. S. Wong, *Small* **2010**, *6*, 412.

[47] J. K. Han, C. McBean, L. Wang, J. Hoy, C. Jaye, H. Q. Liu, Z. Q. Li, M. Y. Sfeir, D. A. Fischer, G. T. Taylor, J. A. Misewich, S. S. Wong, *Chem. Mater.* **2015**, *27*, 778.

[48] A. Kar, A. Datta, A. Patra, *J. Mater. Chem.* **2010**, *20*, 916.

[49] Y. S. Zhu, S. B. Cui, X. Chen, W. Xu, P. W. Zhou, Y. F. Wang, L. Xu, H. W. Song, L. Huang, W. Huang, *Nanoscale* **2014**, *6*, 8075.

[50] C. Yan, A. Dadvand, F. Rosei, D. F. Perepichka, *J. Am. Chem. Soc.* **2010**, *132*, 8868.

[51] A. Fallahi, F. A. Taromi, A. Mohebbi, J. D. Yuen, M. Shahinpoor, *J. Mater. Chem. C* **2014**, *2*, 6491.

[52] B. Geffroy, P. le Roy, C. Prat, *Polym. Int.* **2006**, *55*, 572.

[53] X. S. Fang, Y. Bando, D. Golberg, *J. Mater. Sci. Technol.* **2008**, *24*, 512.

[54] K. Sooklal, B. S. Cullum, S. M. Angel, C. J. Murphy, *J Phys Chem.* **1996**, *100*, 4551.

[55] A. A. Bol, A. Meijerink, *Phys. Rev. B* **1998**, *58*, 15997.

[56] F. Zhang, S. S. Wong, *Chem. Mater.* **2009**, *21*, 4541.

[57] B. Xia, I. W. Lenggoro, K. Okuyama, *Chem. Mater.* **2002**, *14*, 4969.

[58] L. Qu, X. Peng, *J. Am. Chem. Soc.* **2002**, *124*, 2049.

[59] Z. Pan, K. Zhao, J. Wang, H. Zhang, Y. Feng, X. Zhong, *ACS Nano* **2013**, *7*, 5215.

[60] I. Robel, M. Kuno, P. V. Kamat, *J. Am. Chem. Soc.* **2007**, *129*, 4136.

[61] G. S. Li, D. Q. Zhang, J. C. Yu, *Environ. Sci. Technol.* **2009**, *43*, 7079.

[62] X. H. Peng, J. A. Misewich, S. S. Wong, M. Y. Sfeir, *Nano Lett.* **2011**, *11*, 4562.

[63] X. H. Peng, M. Y. Sfeir, F. Zhang, J. A. Misewich, S. S. Wong, *J. Phys. Chem. C* **2010**, *114*, 8766.

[64] S. Banerjee, S. S. Wong, *J. Am. Chem. Soc.* **2003**, *125*, 10342.

[65] X. H. Peng, J. Y. Chen, J. A. Misewich, S. S. Wong, *Chem. Soc. Rev.* **2009**, *38*, 1076.

[66] S. Banerjee, S. S. Wong, *Nano Lett.* **2002**, *2*, 195.

[67] K. S. Leschkies, R. Divakar, J. Basu, E. Enache-Pommer, J. E. Boercker, C. B. Carter, U. R. Kortshagen, D. J. Norris, E. S. Aydil, *Nano Lett.* **2007**, *7*, 1793.

[68] I. Robel, V. Subramanian, M. Kuno, P. V. Kamat, *J. Am. Chem. Soc.* **2006**, *128*, 2385.

[69] C. S. Lewis, H. Liu, J. Han, L. Wang, S. Yue, N. A. Brennan, S. S. Wong, *Nanoscale* **2016**, *8*, 2129.

[70] A. D. Dinsmore, D. S. Hsu, S. B. Qadri, J. O. Cross, T. A. Kennedy, H. F. Gray, B. R. Ratna, *J. Appl. Phys.* **2000**, *88*, 4985.

[71] B. Katircioglu, J. L. Pautrat, D. Bensahel, N. Magnea, *Radiat. Eff.* **1978**, *37*, 183.

[72] G. J. Lee, S. Anandan, S. J. Masten, J. J. Wu, *Ind. Eng. Chem. Res.* **2014**, *53*, 8766.

[73] G. Wang, B. B. Huang, Z. J. Li, Z. Z. Lou, Z. Y. Wang, Y. Dai, M. H. Whangbo, *Sci. Rep.* **2015**, *5*, 5844.

[74] A. A. Bol, A. Meijerink, *Phys. Rew. B* **1998**, *58*.

[75] J. F. Suyver, S. F. Wuister, J. J. Kelly, A. Meijerink, *Nano Lett.* **2001**, *1*, 429.

[76] R. Rossetti, R. Hull, J. M. Gibson, L. E. Brus, *J. Chem. Phys.* **1985**, *82*, 552.

[77] D. Denzler, M. Olschewski, K. Sattler, *J. Appl. Phys.* **1998**, *84*, 2841.

[78] J. Han, L. Wang, S. S. Wong, *J. Phys. Chem. C* **2014**, *118*, 5671.

[79] K. T. Shimizu, W. K. Woo, B. R. Fisher, H. J. Eisler, M. G. Bawendi, *Phys. Rev. Lett.* **2002**, *89*, 117401.

[80] H. S. Bhatti, R. Sharma, N. K. Verma, N. Kumar, S. R. Vadera, K. Manzoor, *J. Phys. D: Appl. Phys.* **2006**, *39*, 1754.

[81] D. R. James, Y. S. Liu, P. Demayo, W. R. Ware, *Chem. Phys. Lett.* **1985**, *120*, 460.

[82] J. Jasieniak, M. Califano, S. E. Watkins, *ACS Nano* **2011**, *5*, 5888.

[83] B. T. Luong, E. Hyeong, S. Yoon, J. Choi, N. Kim, *RSC Adv.* **2013**, *3*, 23395.

[84] C. S. McCamy, *Color Res. Appl.* **1992**, *17*, 142.

Figure Captions

Figure 1. XRD patterns of (A) as-prepared and (B) annealed ZnS: Mn^{2+} NWs.

Figure 2. (A, B) TEM images, (C) HRTEM image, and (D) associated SAED pattern for as-prepared (prior to thermal annealing) Zn: Mn^{2+} NWs.

Figure 3. (A, B) TEM images, (C) HRTEM image, and (D) the associated SAED pattern for Zn: Mn^{2+} NWs, after annealing.

Figure 4. (A, B) TEM images, (C) HRTEM images, and (D) the associated SAED pattern for ZnS: Mn^{2+} - AET-capped CdSe QD heterostructures.

Figure 5. (A) Dark-field STEM image recorded on a set of adjoining ZnS: Mn^{2+} - AET-capped CdSe QD nanoscale heterostructures. (B−F) Elemental EDS mapping of the same region of nanowires, highlighting the overlapping spatial chemical distribution of Zn (B, green), S (C, blue), Mn (D, red), Cd (E, pink), and Se (F, gold), respectively. Scale bar is 1 μm in every image.

Figure 6. UV-visible spectra of ZnS: Mn^{2+} NWs (black), AET-capped CdSe QDs (blue), as well as the corresponding ZnS: Mn^{2+} NW - AET-capped CdSe QD heterostructures (red), respectively.

Figure 7. PL emission spectra indicate quenching of (A) ZnS: Mn^{2+} emission and a slight enhancement of the (B) CdSe QD emission within the corresponding, as-prepared heterostructures. Excitation wavelengths are located at 350 nm.

Figure 8. PL emission spectra of ZnS: Mn^{2+} - AET-capped CdSe QD heterostructures, possessing [ZnS: Mn^{2+}]: [AET-capped CdSe QD] ratios of 1: 1.5 (red) and 1: 3 (blue), respectively.

Figure 9. PL decay curve (dots) (λ_{ex} = 388 nm) with corresponding fitting curves (line) associated with (A) ZnS self-activated emission, (B) Mn^{2+} dopant-induced emission, as well as (C) AET-capped CdSe QD emission within heterostructures with [ZnS: Mn^{2+}]: [AET-capped QD] ratios, ranging from 1: 1.5 to 1: 3, respectively.

Figure 10. Diagram of energy level alignments of ZnS: Mn^{2+} - AET-capped CdSe QD heterostructures with labeled charge transfer pathways (i.e. e^-, as electron transfer; h^+ as hole transfer) as well as energy

transfer channels (ET as energy transfer).

Figure 11. Overlay graph of UV absorption spectrum of as-prepared AET-capped CdSe QDs (black) with the corresponding PL emission spectrum of 1D ZnS: Mn^{2+} (blue). Evident overlap in the 400-500 nm region supports possible energy transfer from ZnS defect sites to QDs within the corresponding heterostructures.

Figure 12. (A) CIE chromaticity diagram (A) of ZnS: Mn^{2+} - AET-capped CdSe QD heterostructures (2.22%, Mn^{2+}) with control components of 'free', unbound AET-capped CdSe QDs (green), pristine ZnS: Mn^{2+} (black) and undoped ZnS NWs (blue) shown. (B) CIE chromaticity diagram with labeled CCT values associated with corresponding ZnS: Mn^{2+}- AET-capped CdSe QD heterostructures (molar ratio of 1: 1.5) with actual Mn^{2+} doping ratios of 0% (black), 0.45% (blue), 1.19% (cyan), 1.51% (green), 1.75% (yellow), and 2.22% (red), respectively.

Table 1. Summary of quenched intensities in terms of the percentages of ZnS and Mn^{2+} emission within corresponding heterostructures with host: QD molar ratios of 1: 3 and 1: 1.5, respectively. Higher Q_{ZnS} as opposed to Q_{Mn} values result from the additional energy transfer from ZnS onto immobilized CdSe QDs.

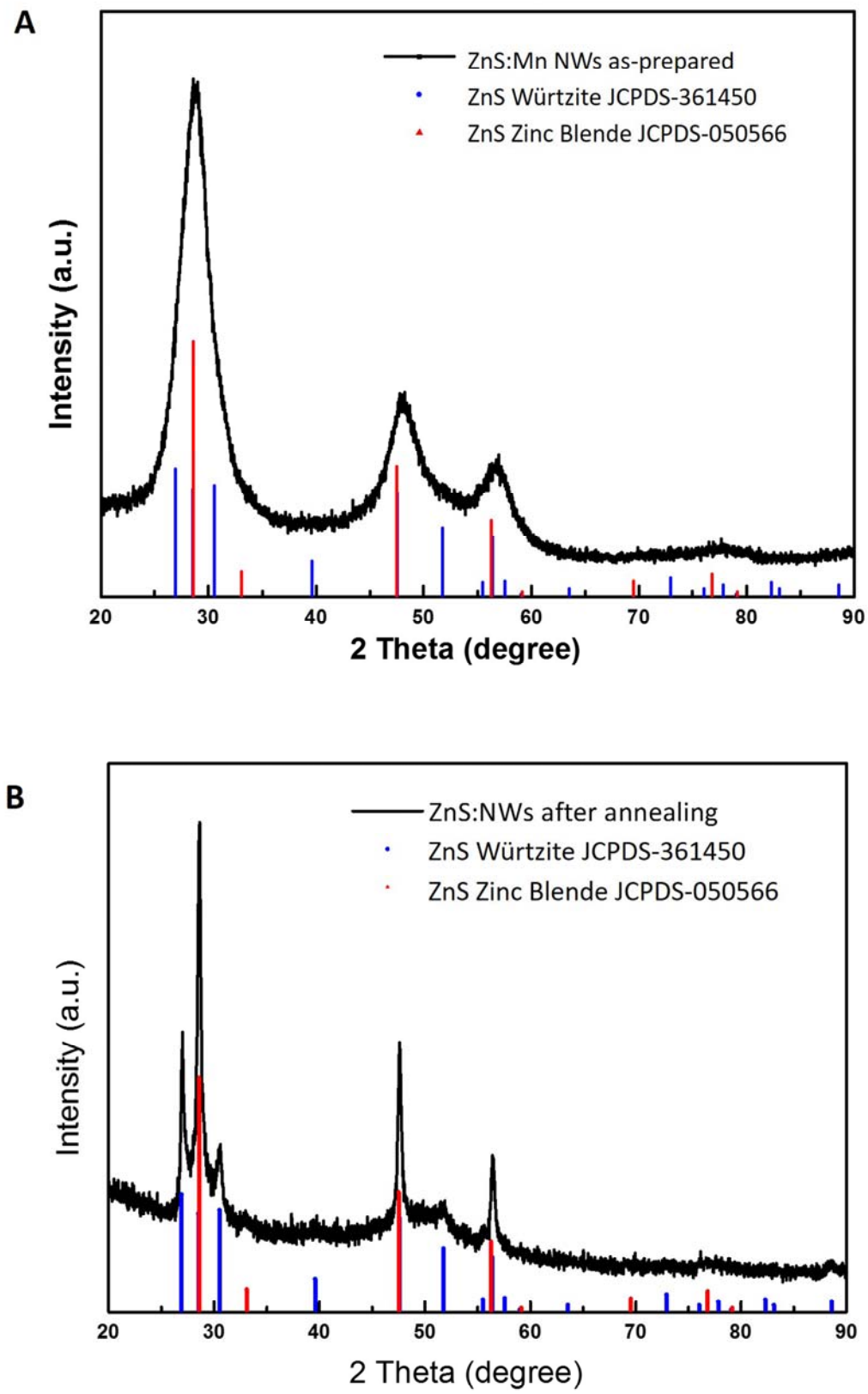
A
ZnS:Mn NWs as-prepared
ZnS Würtzite JCPDS-361450
ZnS Zinc Blende JCPDS-050566
Intensity (a.u.)
20
30
40
50
60
70
80
90
2 Theta (degree)
B
ZnS:NWs after annealing
ZnS Würtzite JCPDS-361450
ZnS Zinc Blende JCPDS-050566
Intensity (a.u.)
20
30
40
50
60
70
80
90
2 Theta (degree)

Figure 1.

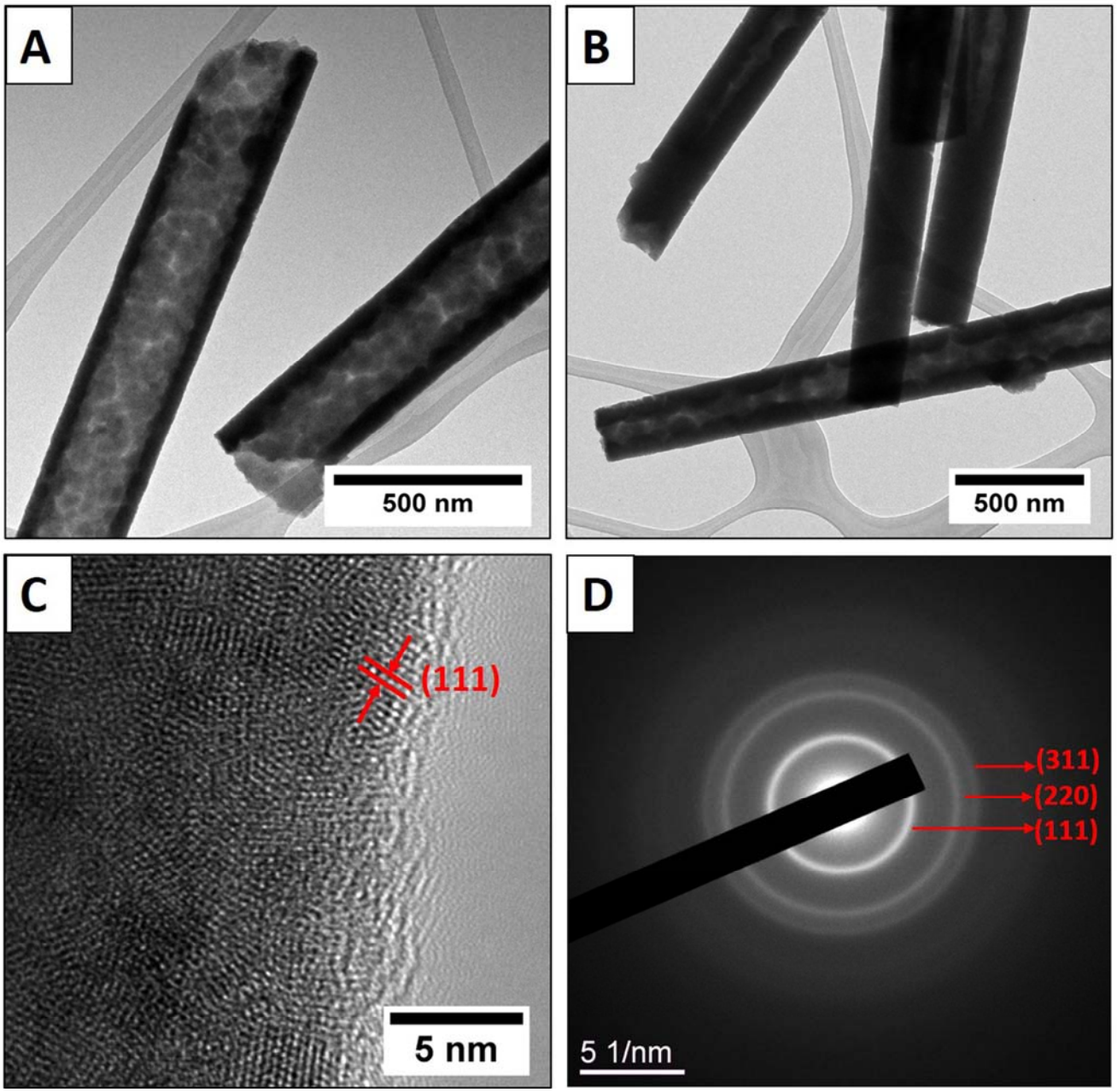

Figure 2.

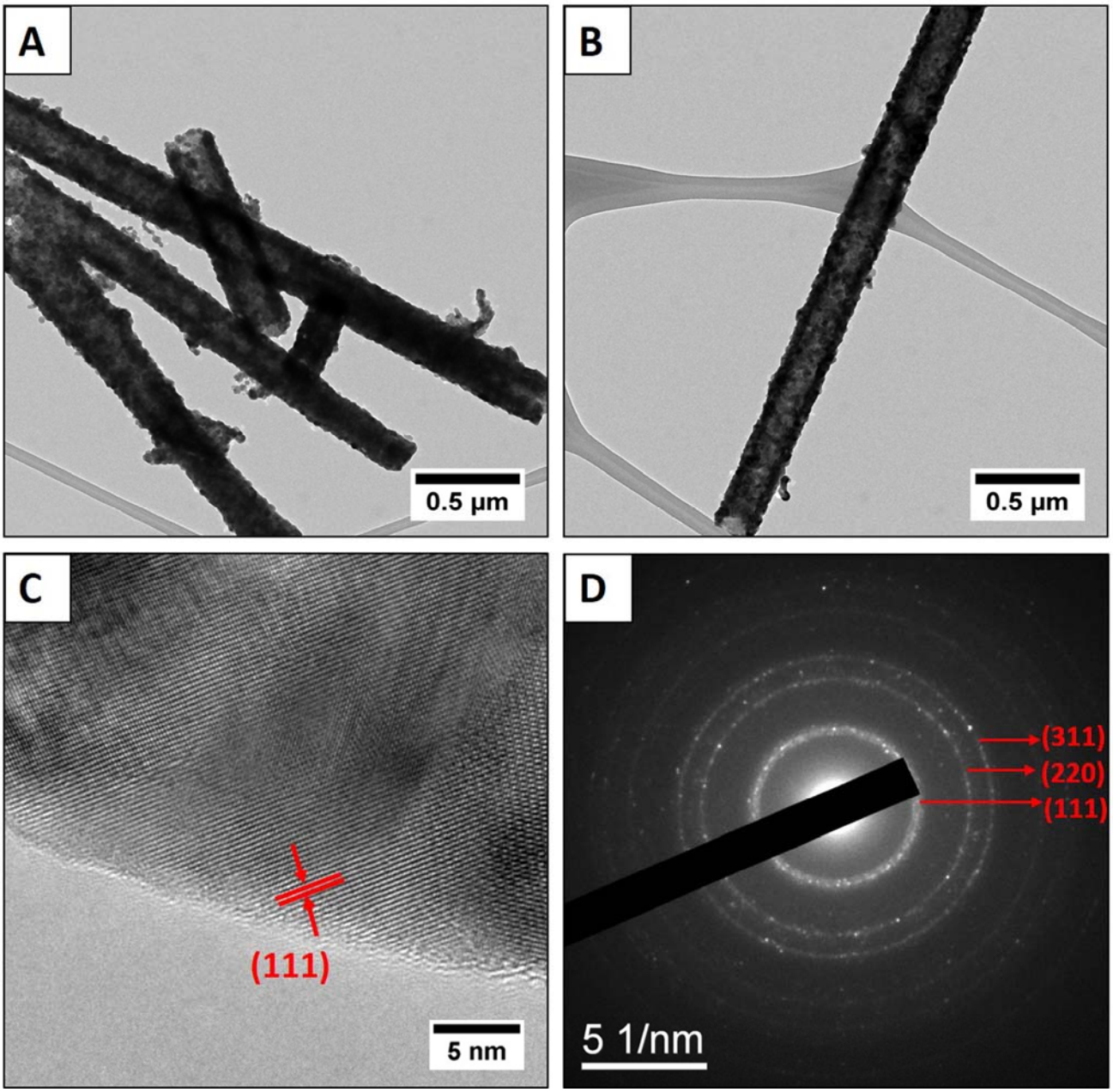

Figure 3.

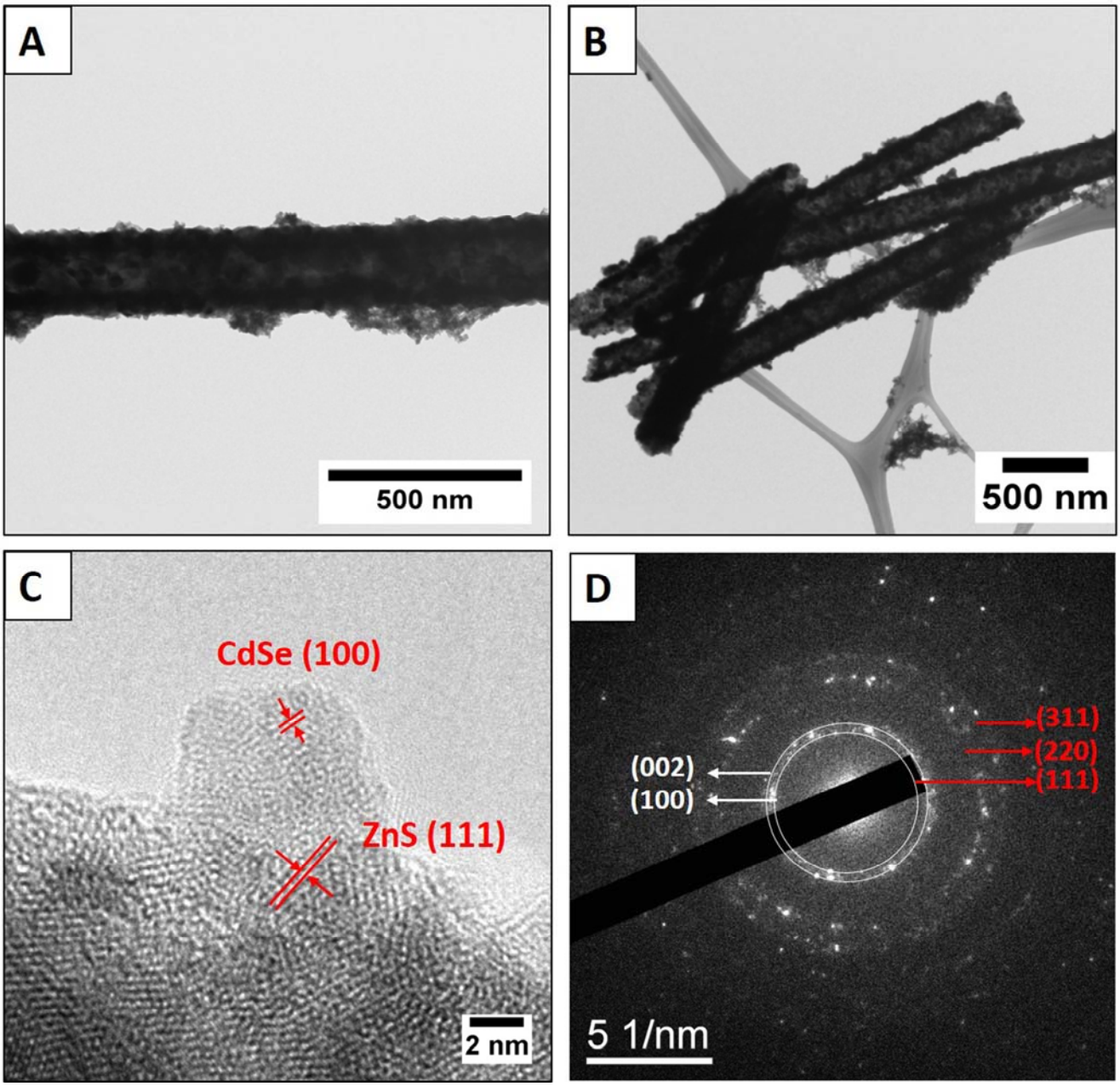

Figure 4.

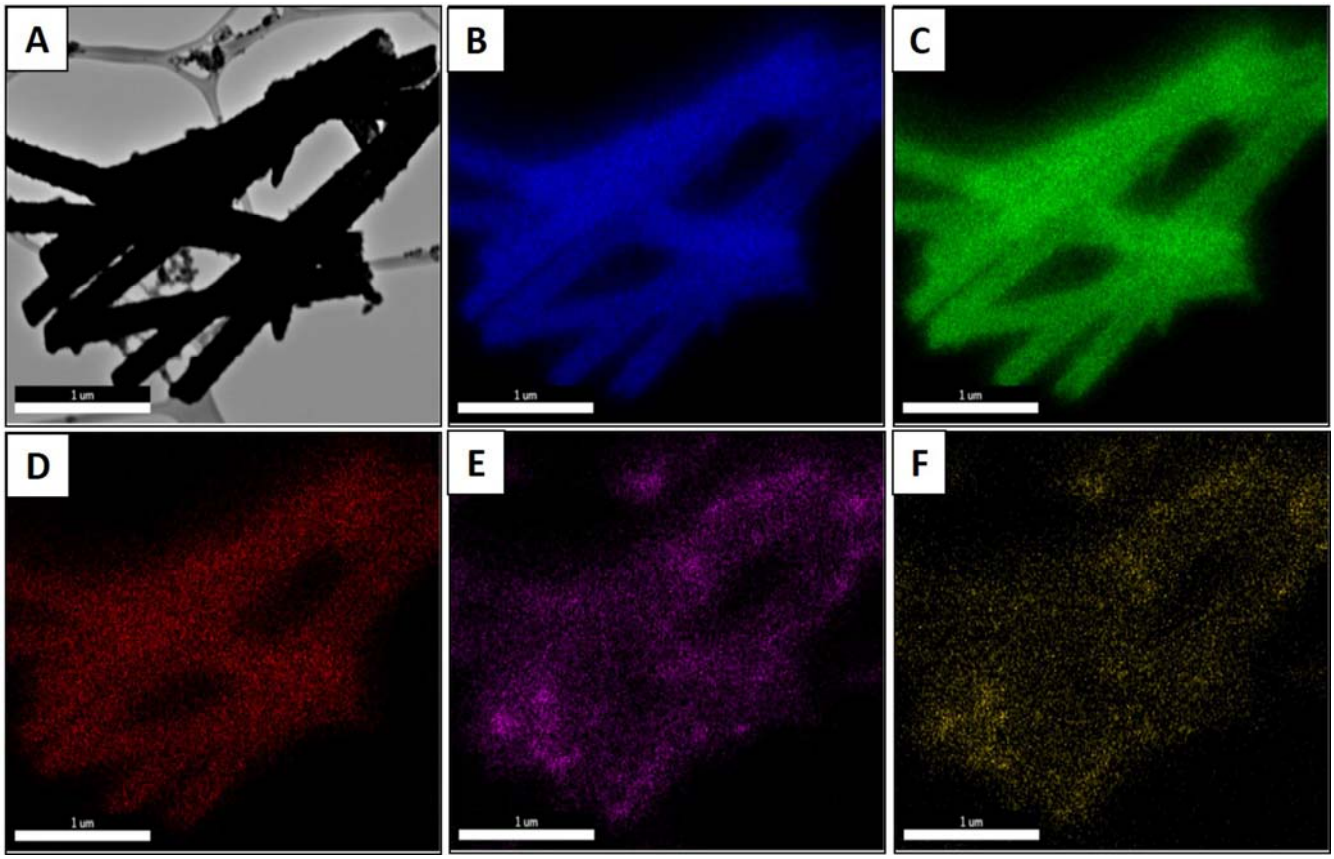

Figure 5.

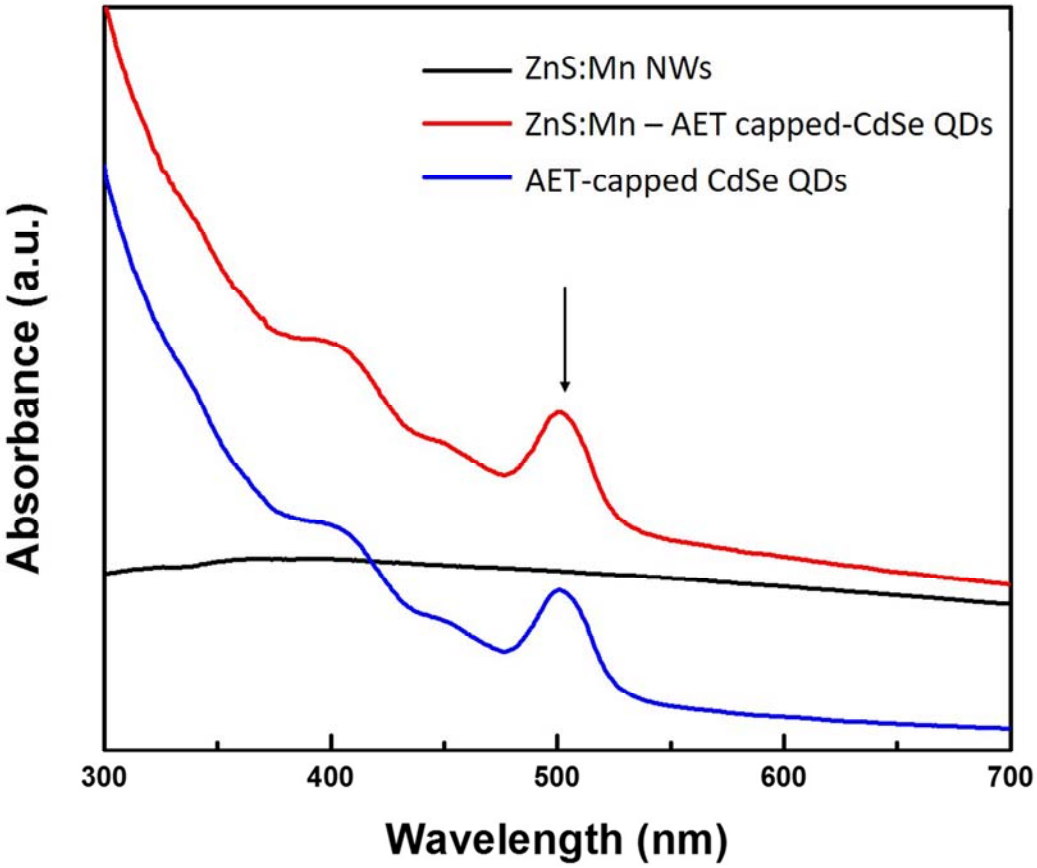
ZnS:Mn NWs
ZnS:Mn – AET capped-CdSe QDs
AET-capped CdSe QDs
Absorbance (a.u.)
300
400
500
600
700
Wavelength (nm)

Figure 6.

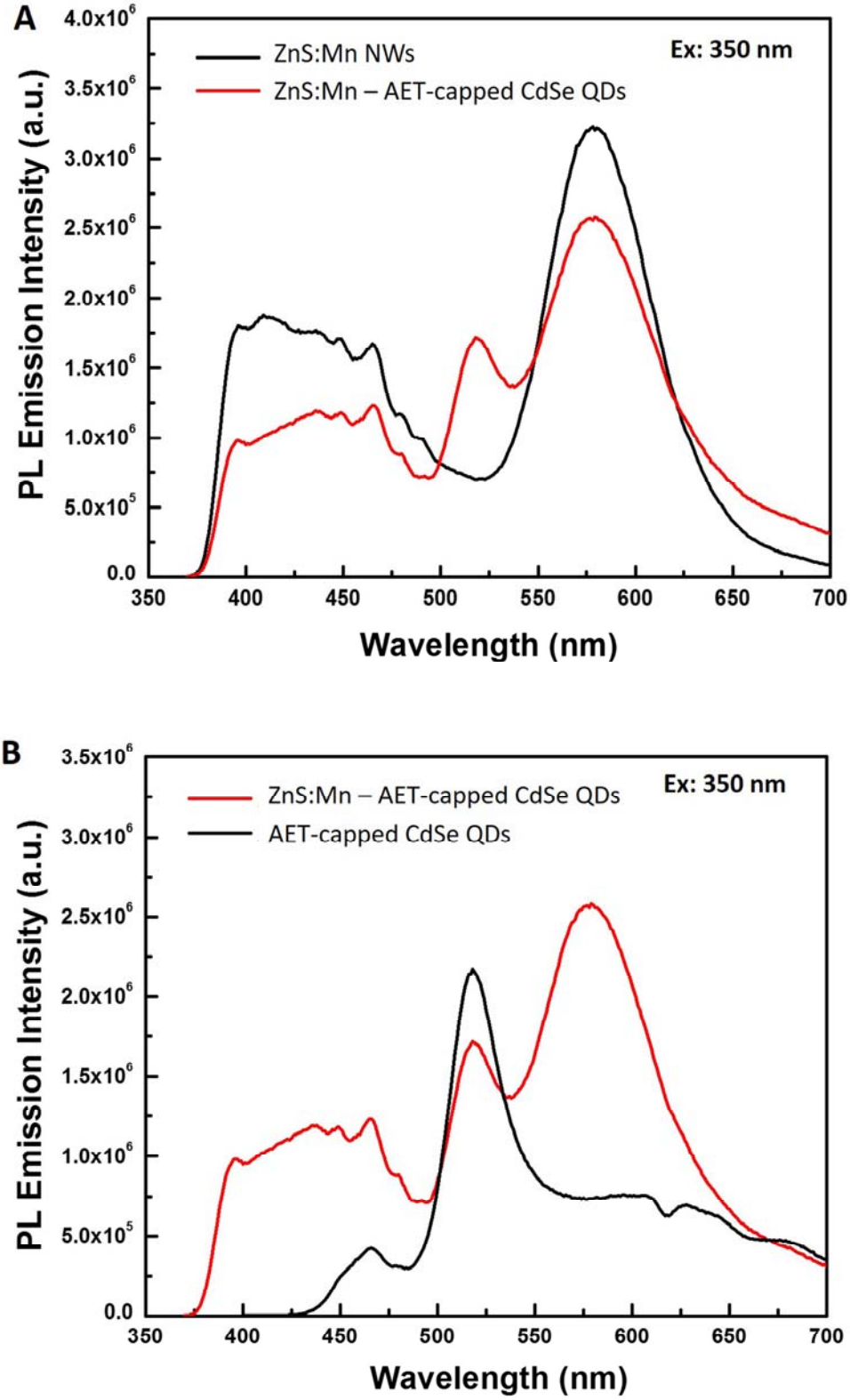
A
ZnS:Mn NWs
ZnS:Mn – AET-capped CdSe QDs
Ex: 350 nm
PL Emission Intensity (a.u.)
Wavelength (nm)
B
ZnS:Mn – AET-capped CdSe QDs
AET-capped CdSe QDs
Ex: 350 nm
PL Emission Intensity (a.u.)
Wavelength (nm)

Figure 7.

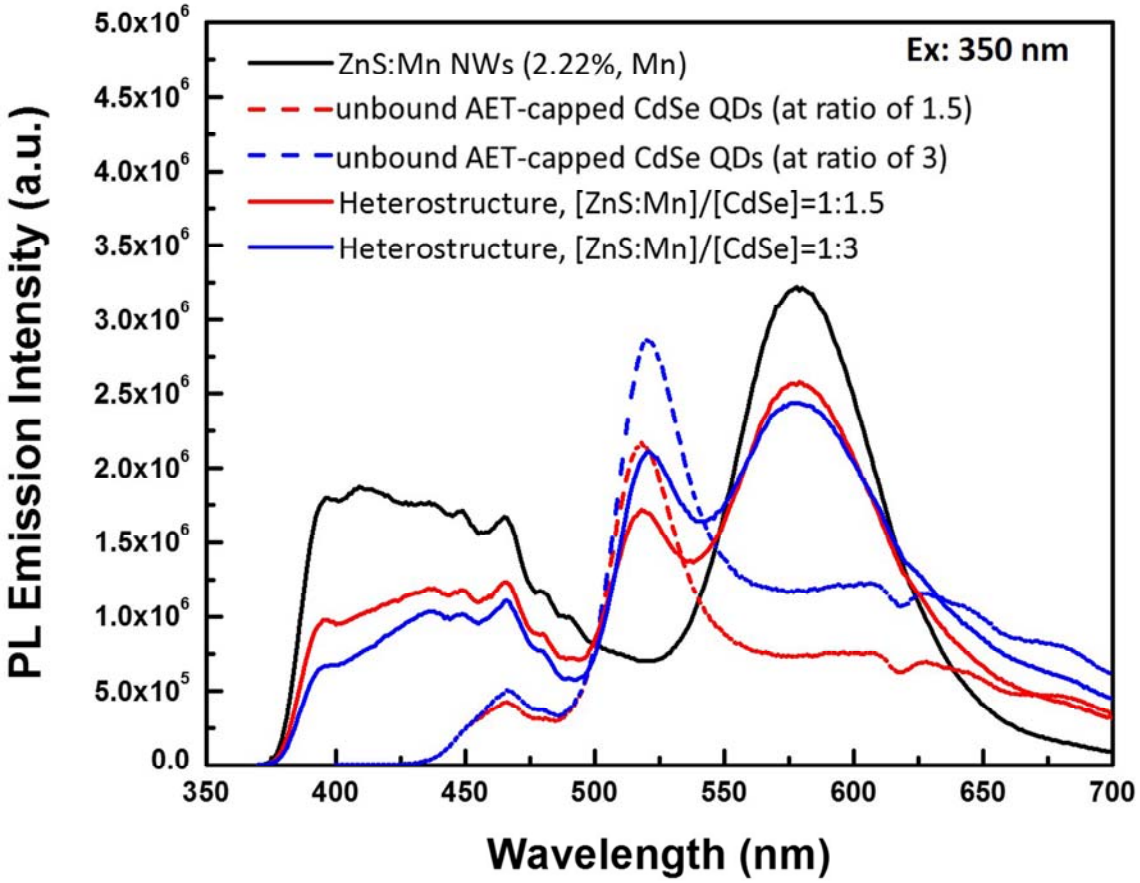
Ex: 350 nm
ZnS:Mn NWs (2.22%, Mn)
unbound AET-capped CdSe QDs (at ratio of 1.5)
unbound AET-capped CdSe QDs (at ratio of 3)
Heterostructure, [ZnS:Mn]/[CdSe]=1:1.5
Heterostructure, [ZnS:Mn]/[CdSe]=1:3
PL Emission Intensity (a.u.)
Wavelength (nm)
5.0x10^6
4.5x10^6
4.0x10^6
3.5x10^6
3.0x10^6
2.5x10^6
2.0x10^6
1.5x10^6
1.0x10^6
5.0x10^5
0.0
350
400
450
500
550
600
650
700

Figure 8.

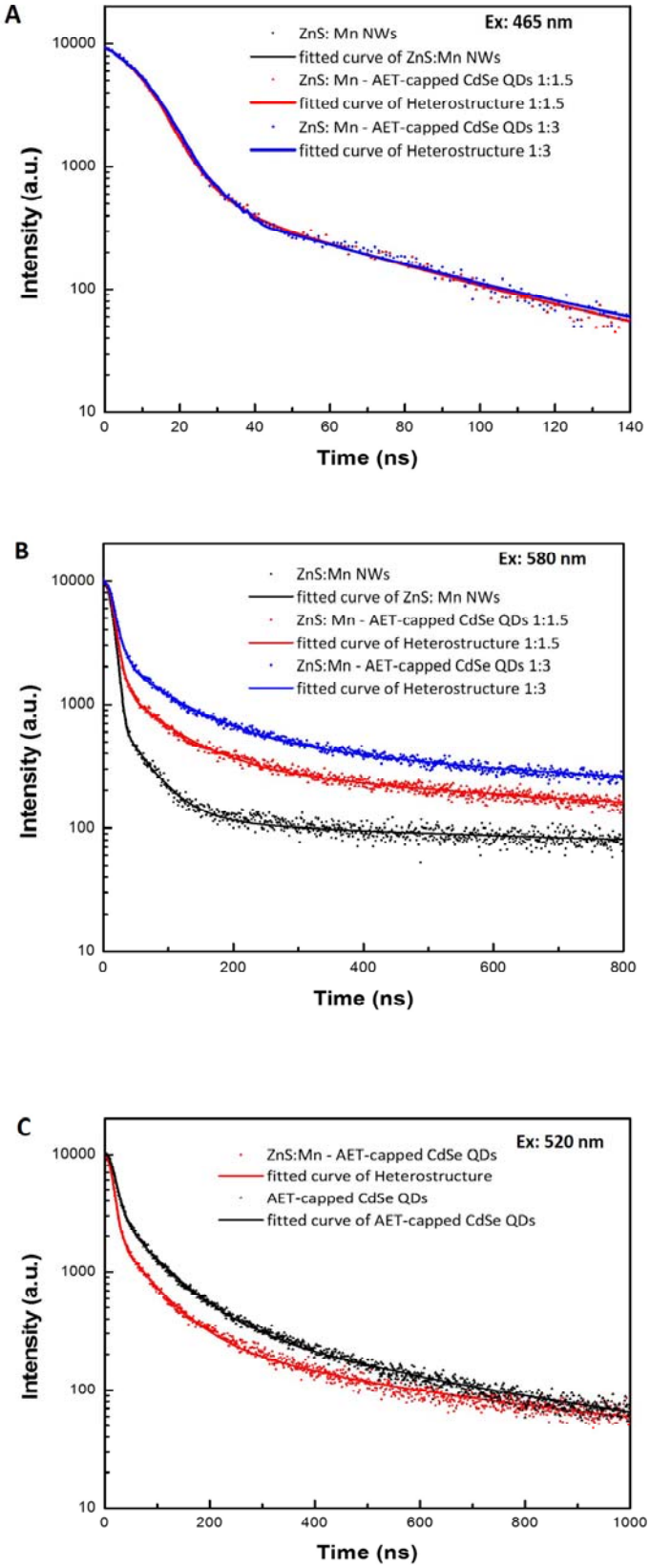
A
Ex: 465 nm
ZnS: Mn NWs
fitted curve of ZnS:Mn NWs
ZnS: Mn - AET-capped CdSe QDs 1:1.5
fitted curve of Heterostructure 1:1.5
ZnS: Mn - AET-capped CdSe QDs 1:3
fitted curve of Heterostructure 1:3
Intensity (a.u.)
Time (ns)
B
Ex: 580 nm
ZnS:Mn NWs
fitted curve of ZnS: Mn NWs
ZnS: Mn - AET-capped CdSe QDs 1:1.5
fitted curve of Heterostructure 1:1.5
ZnS:Mn - AET-capped CdSe QDs 1:3
fitted curve of Heterostructure 1:3
Intensity (a.u.)
Time (ns)
C
Ex: 520 nm
ZnS:Mn - AET-capped CdSe QDs
fitted curve of Heterostructure
AET-capped CdSe QDs
fitted curve of AET-capped CdSe QDs
Intensity (a.u.)
Time (ns)

Figure 9.

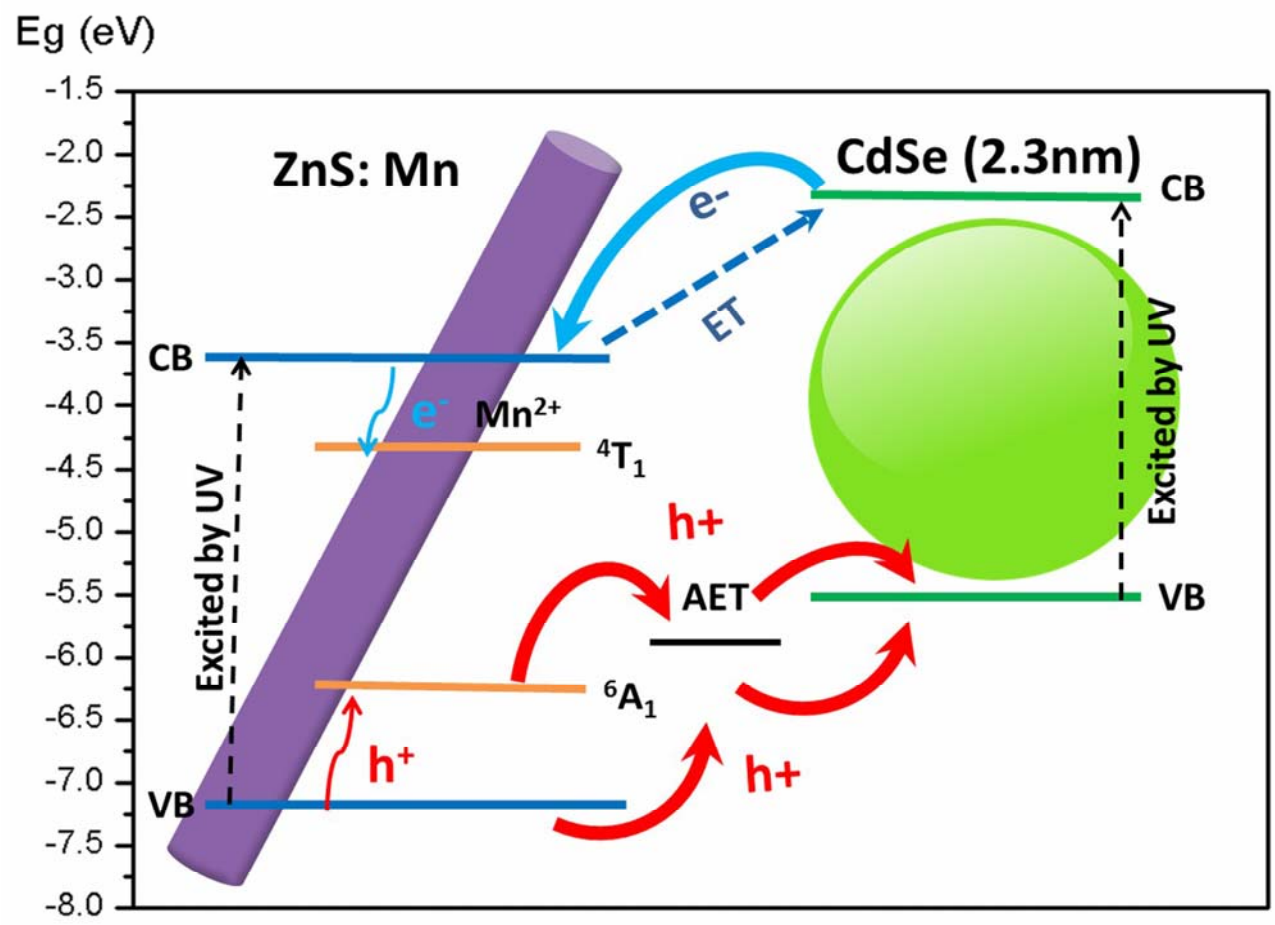
Eg (eV)
-1.5
-2.0
-2.5
-3.0
-3.5
-4.0
-4.5
-5.0
-5.5
-6.0
-6.5
-7.0
-7.5
-8.0
ZnS: Mn
CdSe (2.3nm)
CB
e-
ET
CB
e-
Mn2+
4T1
Excited by UV
h+
AET
VB
Excited by UV
6A1
h+
h+
VB

Figure 10.

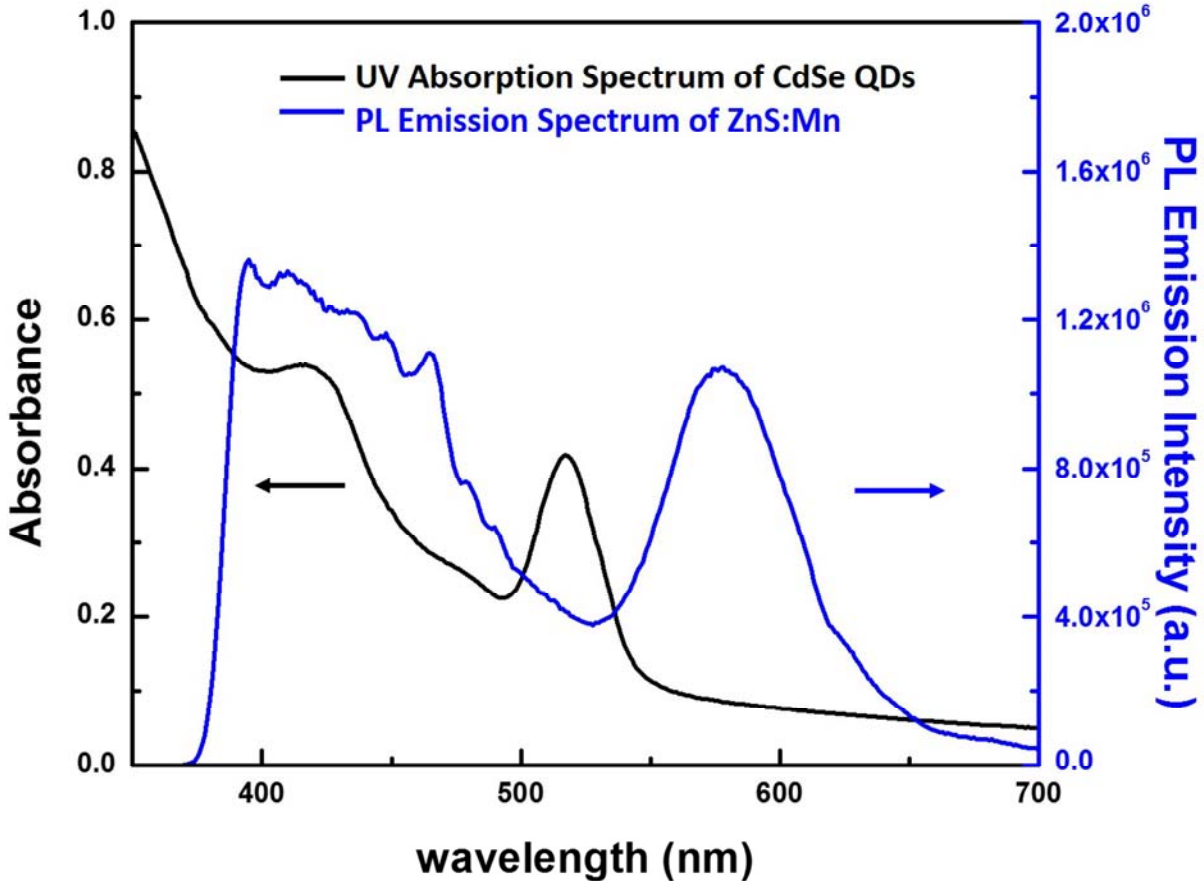
UV Absorption Spectrum of CdSe QDs
PL Emission Spectrum of ZnS:Mn
Absorbance
PL Emission Intensity (a.u.)
wavelength (nm)
1.0
0.8
0.6
0.4
0.2
0.0
2.0x10^6
1.6x10^6
1.2x10^6
8.0x10^5
4.0x10^5
0.0
400
500
600
700

Figure 11.

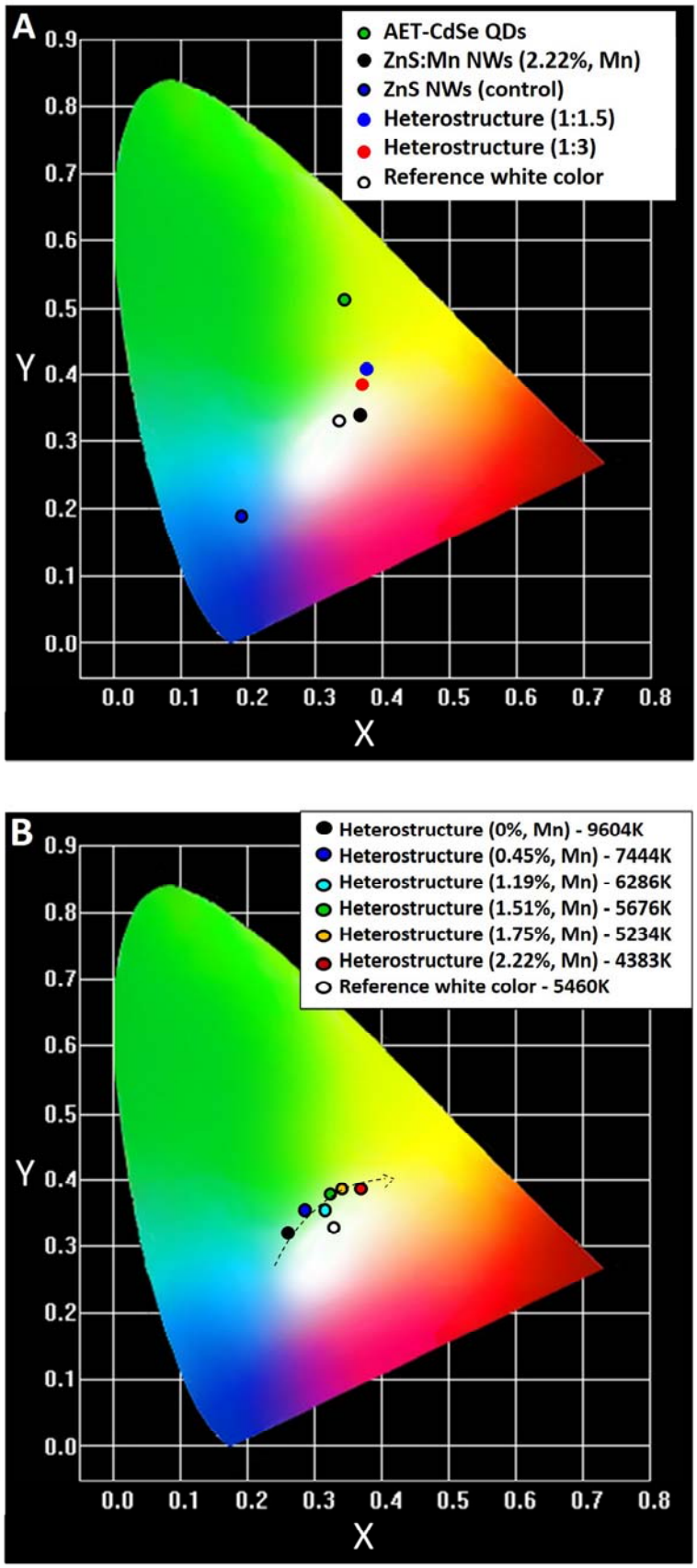
A
AET-CdSe QDs
ZnS:Mn NWs (2.22%, Mn)
ZnS NWs (control)
Heterostructure (1:1.5)
Heterostructure (1:3)
Reference white color
Y
X
0.0
0.1
0.2
0.3
0.4
0.5
0.6
0.7
0.8
0.9
B
Heterostructure (0%, Mn) - 9604K
Heterostructure (0.45%, Mn) - 7444K
Heterostructure (1.19%, Mn) - 6286K
Heterostructure (1.51%, Mn) - 5676K
Heterostructure (1.75%, Mn) - 5234K
Heterostructure (2.22%, Mn) - 4383K
Reference white color - 5460K

Figure 12.

QD coverage – Molar ratios of [ZnS: Mn^{2+}]: [AET-capped CdSe QD]	**Percentage of the quenched intensity of ZnS emission (Q_{ZnS})**	**Percentage of the quenched intensity of Mn^{2+} emission (Q_{Mn})**
1: 3	58.4 %	44.3 %
1: 1.5	44.8 %	35.1 %

Table 1.